Review article

The catalyst layer and its dimensionality — A look into its ingredients and how to characterize their effects

Nada Zamel

Fraunhofer Institute for Solar Energy Systems ISE, Freiburg, Germany

HIGHLIGHTS

- A review of catalyst layer ink ingredients is given.
- Ionomer as a binder and its effect are discussed.
- Alternative supports to the traditional carbon are discussed.
- Alloyed Pt catalysts and Pt-free catalysts are discussed.
- Characterization techniques are listed.

ARTICLE INFO

ABSTRACT

Development of polymer electrolyte membrane (PEM) fuel cells throughout the years is established through its component optimization. This is especially true of its catalyst layer, where structuring of the layer has led to many breakthroughs. The catalyst layer acts as the heart of the cell, where it controls the half-cell reactions and their products. The complex nature of various transport phenomena simultaneously taking place in the layer requires the layer to be heterogeneous in structure. Hence, a delicate balance of the layer's ingredients, coupled with the understanding of the ingredients' interaction, is required. State-of-the-art catalyst layers are composed of a catalyst, its support, a solvent and a binder. Changes in the morphology, structure or material of any of these components ultimately affects the layer's activity and durability. In this review paper, we provide an overview of the various works tailored to understand how each component in the catalyst's ink affects the stability and life-time of the layer.

© 2016 Elsevier B.V. All rights reserved.

1. Introduction

Advancement in polymer electrolyte membrane (PEM) fuel cells, specifically for automotive applications, has been achieved through systematic optimization of its components. The use of thinner components, specifically the membrane, and the use of structured catalyst layers are two of the main breakthroughs in this advancement. The importance of the catalyst layer to PEM fuel cells is dictated by its functions and its location between the porous transport layer (PTL) and the electrolyte membrane. As the area where the electrochemical half-cell reactions occur, it must provide continuous pathways for various species; primarily, (i) a continuous path for efficient transport of protons, (ii) continuous pore network for the transport of reactants/products and for efficient

water removal and (iii) continuous passage for the conduction of electrons between the catalyst layer and the current collector. In turn, the catalyst layer's structure is heterogeneous and complex and its optimization is required for the increase of its activity and the performance of the cell. This is further complicated by the requirement for its stability and durability over the lifetime of the cell and under various operating conditions.

The interconnection between structure optimization and the increase in power density of the cell is highlighted through the history of catalyst layer preparation. Methods for preparing conventional catalyst layers date back to 1967, when Niedrach [1] used polytetrafluoroethylene (PTFE) as the binder to hold fine powder metal catalyst particles together. However, proton conduction was lacking within these PTFE-bonded catalyst layers as Raistrick later showed [2]. Hence, a method of impregnating Nafion® solution through the surface of a finished catalyst layer was developed. This was a breakthrough in which it highlighted the importance of a 3-

E-mail address: nada.zamel@ise.fraunhofer.de.

phase interface. Brushing a Nafion® solution on the electrode surface to introduce Nafion® within the catalyst layer was later developed by Ticianelli et al. [3]. Uchida et al. [4] utilized the colloidal method to mix a perfluorosulfonated ionomer directly with the catalyst powder; however, still used PTFE as the binder. The use of PTFE as the binder required high Pt loadings. The main breakthrough came when Wilson and Gottesfeld [5,6] eliminated the use of PTFE all together by using recast Nafion® ionomer as the binder and significantly reduced the amount of Pt loadings. Subsequently, Pt-black, i.e. unsupported Pt, was replaced with Pt supported on carbon to reduce the metal content. The structure of this state-of-the-art catalyst layer, Fig. 1(a), is typically formed by the dispersion of an ink comprising a catalyst deposited onto a support (e.g. Pt/C), binder (e.g. PFSA ionomer) and a dispersing solvent. The structure of the layer is, hence, shaped within the ink by the agglomeration of the carbon particles and the aggregation of the ionomer. The dispersion medium governs the ink's properties, such as aggregation size of the catalyst/ionomer particles, viscosity, rate of solidification and ultimately the physical and mass transport properties of the catalyst layer [8]. In this case, the binder material used in the preparation of the ink is required to be a proton conductor. Any imbalance in the amount of the ionomer in the catalyst layer can result in transport losses. Too little ionomer results in poor ionic conductivity and reduced active sites, while too much results in flooding of the layer and ultimately, slow diffusion of the gases to the reactant sites. Understanding how the ionomer distributes within the catalyst layer is important in optimization studies of the layer and there is great evidence in literature that points to the aggregation of the ionomer solution [8,9]. Durability and stability of the catalyst layer is hence governed by its catalyst utilization, rate of support degradation (e.g. carbon corrosion) and ionomer stability [10,11].

Efforts to increase the stability of the catalyst layer are always ongoing with some focused on increasing the durability of various components, such as the binder or the support and others on finding alternative preparation methods. The latter is achieved by looking at decreasing the catalyst layer's thickness by eliminating one or more of the ingredients mentioned earlier. An example of such efforts are catalyst layers fabricated by the dispersion of Pt on the gas diffusion layer or dispersion of Pt/C on the electrolyte membrane, forming a very thin layer between the PTL and the electrolyte membrane [12–14]. Another such example are ultra-thin catalyst layers (UTCL) or nano-structured thin film (NSTF) catalyst layers. These catalyst layers are ionomer-free and are often composed of nanostructured support, such as gold or carbon, on which the catalyst is dispersed. The 3 M thin film catalyst layer, Fig. 1(b), is in the forefront of research and has shown high catalytic activity and very high stability and durability. The catalyst is supported on thin whiskers manufactured from an organic material, Perylene red 149, which does not take part in the transport phenomena within the layer. The 3 M catalyst layer contains neither carbon nor additional ionomer and thus, durability issues due to carbon corrosion and ionomer degradation are eliminated [11]. However, as discussed later in this paper, other issues with such a catalyst structure arise. Other efforts have been focused on fabricating structured catalyst layers. In Ref. [15], Zhang and Shi combined the benefits of using PTFE and ionomer as a binder in fabricating a dual-bonded catalyst layer. With using a structured catalyst layer using an ionomer-bonded and PTFE-bonded catalyst layer, they reported an improvement of about 25% in the electric yield rate. Dual-layer structured electrodes have also been investigated in Ref. [16], where the effect of varying PTFE content as well as layer thicknesses was examined. In Ref. [17], Su and co-workers structured the catalyst layer by fabricating a double catalyst layer
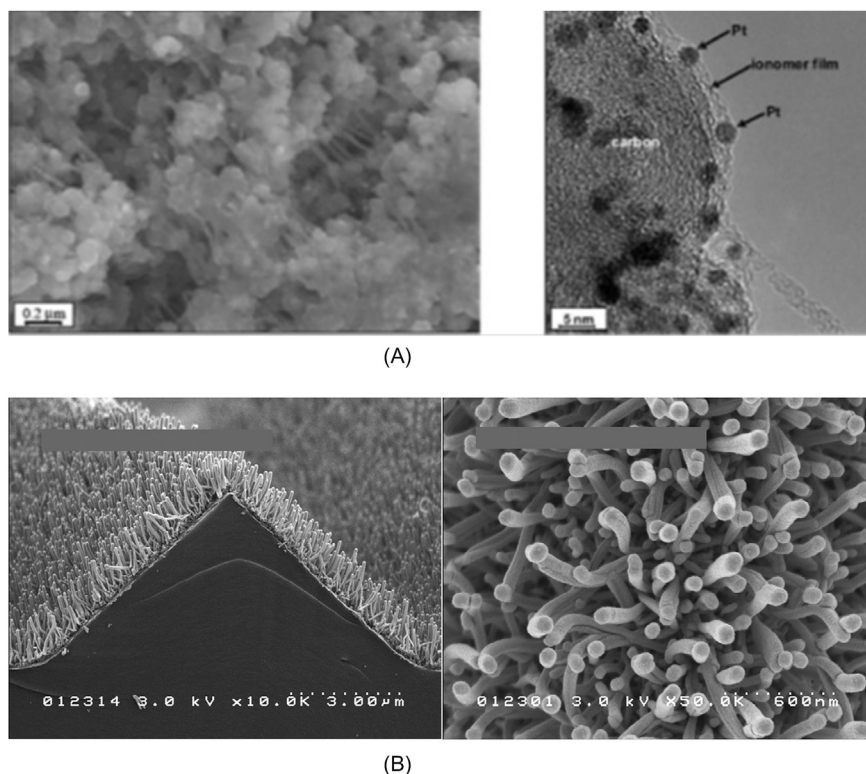

(A)

(B)

Fig. 1. (a) SEM (left) and TEM images (right) showing catalyst layer and ionomer strands that bind Pt/C agglomerates and an ionomer film, respectively [7] *Reproduced from Ref.* [7] *with permission from the Electrochemical Society*; (b) Scanning electron micrographs of typical NSTF catalysts as fabricated on a micro-structured catalyst transfer substrate, seen (left) in cross section with original magnification of X 10,000, and (right) in plane view with original magnification of X 50,000 *Reproduced from Ref.* [21] *with permission from Elsevier.*

where the Pt distribution varied from the GDL surface to the electrolyte membrane. They investigated various distribution ratio of Pt and found that the ratio of thickness as well as Pt have an effect on the overall utilization of Pt. Three-dimensional, ordered macroporous structures have also been investigated to be used to structure the catalyst layer of fuel cells [18–20]. If successfully fabricated, this type of electrode provides a robust and integrated configuration of the catalyst layer; hence, is able to maintain its structural and effective properties. In Ref. [18], Kim et al. reported a direct application of such an electrode where the performance of the inverse opal electrode was successfully demonstrated in a single PEM fuel cell.

In Ref. [21], a detailed overview of various preparation techniques is given where the classification of the catalyst layer is made in terms of the preparation of ink and the dispersion technique. The main considerations of a catalyst ink, regardless of the catalyst layer type, are its contents, its uniformity and its viscosity. The inks are usually either stirred or ultrasonically dispersed thoroughly to ensure contact between the components and the uniformity of the ink. From the overview, conventional catalyst layers are classified into hydrophobic and hydrophilic electrodes, while the non-conventional are classified as deposition electrodes as summarized in Table 1.

Despite differences in structure of various catalyst layers investigated in literature, the common aspect of these layers is that optimization of the structure leads to optimization of the performance. The optimization of the structure is directly affected by the transport properties of the various components of the layer. In this manuscript, emphasis is put towards discussing the importance of each of the components within the ink and its influence on the catalyst layer's properties. Within state-of-the-art catalyst layers, the interest is often in understanding the binder type, the catalyst type and its support as well as the solvent. The contribution of these four ingredients to transport losses is also of interest. In the next sections of the paper, we review works that shed light onto the factors influencing the properties of these catalyst layers. Further, we give a summary of various physical and electrochemical techniques used to investigate transport in the catalyst layer.

2. The binder

The homogeneity of the catalyst ink and the interaction of its components determine the final structure of the sate-of-the-art catalyst layer. In general, three components are required, catalyst on a support, binder (ionomer) and a solvent. The mixing of these components and the subsequent drying of the ink and its dispersion on either the electrolyte membrane or the PTL must be optimized. A comprehensive review of dispersion methods is given elsewhere [23]. Various application methods are used for coating the ink on the porous transport layer, e.g. spreading, spraying, catalyst powder deposition, ionomer impregnation and electrodeposition, while catalyst decal transfer, evaporation deposition, dry spreading and painting are methods often used to transfer the CL to the electrolyte membrane. Using the dry content of the

various components used in the ink, various properties of the catalyst layer can be calculated. The platinum loading is calculated in g_{pt}/cm^2 as the ratio of the product of the weight percentage of platinum times the amount of ink printed on the sample to the geometric area of the sample:

$$Pt_{loading} = \frac{Pt_{wt.\%} m_{dry-ink}}{A_{sample}} \tag{1}$$

where $Pt_{loading}$ is the loading of Platinum, $Pt_{wt.\%}$ is the weight percentage of platinum, $m_{dry-ink}$ is the mass of the dry ink and A_{sample} is the geometric area of the sample. To keep the platinum loading constant while varying the amount of ionomer, for instance, then the catalyst layer thickness must be varied according to:

$$Pt_{loading} = Pt_{wt.\%} \rho_{dry-ink} t_{catalyst-layer} \tag{2}$$

where $t_{catalyst-layer}$ is the thickness of the catalyst layer.

Alternatively, to keep the platinum loading constant, while varying the amount of ionomer and keeping the catalyst layer's thickness constant, the amount of additives can be changed. This in turn will affect the viscosity of the ink and ultimately, the total porosity of the layer, but not the pore distribution [24].

The amount of binder, e.g. Nafion® ionomer is often defined in terms of mg cm^{-2} according to:

$$\frac{dry\ weight\ of\ Nafion\ ionomer}{geometrical\ area\ of\ the\ electrode} \tag{3}$$

or as wt.% according to:

$$\frac{dry\ weight\ of\ Nafion\ ionomer}{weight\ of Pt/Ccatalyst + dry\ weight\ of\ Nafion\ ionomer} \times 100 \tag{4}$$

Nafion® ionomer is the most widely used binder in the preparation of catalyst layers and hence the word binder used from this point on points towards the Nafion® ionomer. Investigation of the optimum amount of Nafion® has been the focus of a number of research papers [4,25–34]. Using various electrochemical techniques, such as polarization curves, cyclic voltammetry and electrochemical impedance spectroscopy, the optimum ionomer content in the catalyst layer is reported to be approx. 30 wt%. In Ref. [35], the optimum PFSA ionomer wt.% in the electrode was suggested to be dependent on the equivalent weight linearly.

Determining an optimum content is, however, not in itself sufficient for understanding the transport within the catalyst layer. The optimization of the performance of the layer is dependent on structural improvements; hence, requiring the understanding of the transport phenomena in the various components as well as their durability and stability.

The binder is not only used for mechanical stability of the catalyst layer, but also it establishes an ionic connection between the electrolyte membrane and the catalyst layer. Unlike the electrolyte membrane itself, the ionomer must be gas permeable as the

Table 1
Classification of catalyst ink and catalyst layers [22].

Hydrophobic ink	Hydrophilic ink and colloid ink	Catalyst ion solution ink and Pt foil
Hydrophobic electrode → PTFE-bonded hydrophobic CL	*Hydrophilic electrode* → Decal method CL → Direct-spraying CL → Ionomer-pyrolyzed CL → Colloid method CL → PTFE/C addition CL	*Deposition electrode* → Sputtering-deposition CL → NSTF CL → Electrochem.-deposition CL → Chemical-deposition CL → IBAD CL

reactants must first dissolve in the ionomer to reach the reactant sites [36]. The content and type of the binder determine the gas permeability, catalytic activity, durability, wettability and ionic conductivity of the catalyst layer [25]. The state-of-the-art binder used in convectional catalyst layers is Perfluorosulfonic Acid (PFSA) ionomer, Nafion®. However, many hydrocarbon polymers, such as s-PES (sulfonated poly (arylene ether sulfone)), s-PSU (sulfonated polysulfone) and s-PEEK (sulfonated poly ether ketone), are also used and are under development for use as ionomer in PEM fuel cell catalyst layers.

The chemical stability of the binder is crucial for the overall durability of the catalyst layer. In particular, the formation of hydrogen peroxide (H_2O_2) during the ORR reaction on the cathode or oxygen crossover on the anode can result in degradation of the side chains of the ionomer. The stability of the ionomer in the presence of hydrogen peroxide is often evaluated via the Fenton's test.

Proton conduction in the ionomer is governed by the acid and its strength as well as the water content and the morphology of the ionomer. Proton conductivity is hence related to the activity of the protons and the proton mobility, which in turn are dependent on the acid strength and water content. Ion-exchange capacity (IEC) is usually a parameter varied in the study of ionomer materials as it gives a measure of the acid content of the ionomer [8]. Water uptake measurements are carried out and their relationship to the IEC of the material is often established. Low uptake rates imply an incomplete dissociation of the acid and poorly connected hydrophilic channels, while too much water implies excessive swelling and dilution of the proton concentration, despite high proton mobility; thus, conductivity is reduced. This relationship between the conductivity and water uptake has been the focus of various research efforts [35,37–39]. In Tables 2–5, we list some of these efforts where various parameters of both Nafion® and hydrocarbon polymers. In these studies, the effects of IEC, degree of sulfonation and hydration on the proton conduction are investigated for some hydrocarbon polymers and Nafion®. An increase in conductivity with a decrease in the equivalent weight is measured for all polymers. Similarly, an increase in the degree of sulfonation of PEEK polymers results in an increase in the proton conductivity and the water uptake as proton conduction is dependent on the number of acid groups and their association and dissociation capability in water.

The proton conductivity of the ionomer film is often investigated using a recast polymer film on a flat substrate. In Refs. [40,41], the dependence of the conductivity of films of recast Nafion® on the thickness was investigated. Siroma et al. showed that the conductivity of a film with a thickness of 100 nm was approximately an order of magnitude less than that of the bulk material; suggesting that an intrinsic change in the material structure existed [41]. This was also combined with investigation of the activation energy of conduction where they measured an increase in the activation energy as the film thickness decreased. Similar findings were also reported in Ref. [41], where the authors also reported on the dependency of the conductivity on the relative humidity. From their

findings, Paul et al. proposed that under the assumption that the ionomer exists as an "aggregated bundle where the non-polar backbone forms the bundle core and sulfonate groups are projected outwards on the bundle surface, then the interaction between the substrate and Nafion bundle can be characterized by electrostatic interaction and hydrogen bonding between the surface groups and sulfonate group" [41]. The dominant mechanism of proton conduction in the thin film Nafion® ionomer was hence proposed to occur via surface diffusion mechanism [41]. Further, they suggested that strong interaction between the sulfonate group and the surface functional group lessens the water adsorption [41]. The ionic conductivity of thin film Nafion® varied according to temperature and relative humidity, with values reported in Refs. [40,41] between 2.6×10^{-9} and 0.03 S cm^{-1}.

Due to interaction of the ionomer with the catalyst and its support in the catalyst layer itself, the ionic conductivity of the ionomer, can hence be different from that reported in Refs. [40,41]. Various in-situ measurement techniques for the ionic conductivity of the catalyst layer are discussed in Ref. [42]. The use of the impedance spectrum of a H_2/N_2 cell is the most commonly applied method to estimate the proton conductivity in situ. Using this method, the proton conductivity of the catalyst layer was reported to be in the range of $1 \times 10^{-4} - 6 \times 10^{-3}$ S cm^{-1} [43]. In literature, an expression based on the Brugmann estimation of effective properties is used to calculate the proton conductivity within the catalyst layer as follows [44]:

$$\kappa^{eff} = \varepsilon^n \kappa^{bulk} \tag{5}$$

where κ^{eff} and κ^{bulk} are the effective proton conductivity in the CL and bulk electrolyte conductivity, respectively, ε is the ionomer content in the catalyst layer and n > 1 is a structural parameter, which defines the tortuosity of the ionomer and its value varies in literature. The main concern with Equation (5) is the uncertainty surrounding the value of the electrolyte conductivity, κ^{bulk}, where it is unclear which value is to be used, the conductivity of the bulk polymer or the thin layer [42].

Direct measurement of the ionic conductivity of the catalyst layer was undertaken by Hess et al. using a micro-structured electrode scaffold (MES). With this method, a structured catalyst layer was used where the electrolyte potential through the thickness of the catalyst layer was measured [45]. From potential measurements, they calculated the in situ conductivity of the catalyst layer to be ~0.045 S/cm, which they reported to be higher than that typically estimated. They explained that the discrepancy between the ex situ studies and the high conductivity measured in their work can arise due to three reasons. "(1) Water generation within the agglomerates results in non-equilibrium water content levels due to water desorption resistances. (2) Water films surrounding the Nafion provide proton transport bridges that reduce tortuosity and increase local mobility as protons are 5 times more mobile in water than in Nafion [46]. (3) Surface conduction mechanisms and acidic groups on the carbon catalyst support may increase the electrode's conductivity." In Ref. [47], Regner argued that the

Table 2
Proton conductivity, IEC, oxygen permeability (diffusivity and solubility) of Nafion®, s-PEEK and s-PSU at 80 °C, 75% and 50% RH [37].

Ionomer	Loading (wt%)	IEC (meq g^{-1})	RH (%)	Oxygen diffusivity ($\times 10^6$ cm^2 s^{-1})	Oxygen solubility ($\times 10^6$ mol cm^{-3})	Oxygen permeability ($\times 10^{12}$ mol cm^{-1} s^{-1})	In-plane H$^+$ conductivity (mS cm^{-1})
Nafion®	31	0.95 ± 0.05	75	6.2 ± 0.5	0.66 ± 0.08	3.9 ± 0.2	10 ± 1
			50	2.7 ± 0.2	1.1 ± 0.1	2.9 ± 0.2	
s-PEEK	15	1.8 ± 0.2	75	1.4 ± 0.1	0.18 ± 0.05	0.27 ± 0.05	1.6 ± 0.3
			50	1.7 ± 0.2	0.09 ± 0.05	0.15 ± 0.05	
s-PSU	15	1.5 ± 0.1	75	0.25 ± 0.08	1.0 ± 0.5	0.16 ± 0.05	0.75 ± 0.05

Table 3
Proton conductivity, IEC and O_2 permeability of PFSA, s-PEEK and s-PSU at 80 °C and 75% RH [35].

Ionomer	IEC (meq g^{-1})	In-plane H$^+$ conductivity (mS cm^{-1})	O^2 permeability ($\times 10^{12}$ mol cm^{-1} s^{-1})
PFSA 1050	0.95	10 ± 0.33	6.0 ± 2
PFSA 750	1.35	26 ± 1.5	3.4 ± 0.7
SPEEK 450	2.1	5.95 ± 0.15	1 ± 0.2
SPEEK 550	1.75	1.60 ± 0.3	0.8 ± 0.5
SPEEK 750	1.35	1.12 ± 0.15	0.41 ± 0.15
SPSU 650	1.5	0.7 ± 0.1	0.15 ± 0.02

Table 4
Effect of solvent and degree of sulfonation on the conductivity and water uptake of s-PEEK polymers at 25 °C and fully hydrated conditions [38].

Polymer	Solvent	DS	$\sigma_{25\,°C}$ (S/cm)	Water uptake at 25 °C (wt%)
Vitrex® PEEK™	DMF	59	8.7×10^{-4}	20.7
		67	2.0×10^{-3}	21.6
		69	3.8×10^{-3}	23.0
		79	3.6×10^{-3}	29.0
		88	3.3×10^{-3}	47.6
		96	3.5×10^{-3}	94.0
	DMAc	69	2.2×10^{-2}	28.0
		79	3.9×10^{-2}	40.0
		88	5.1×10^{-2}	58.2
		96	1.1×10^{-1}	90.1
Gatone™ PEEK	DMF	48	6.8×10^{-4}	14.1
		58	2.5×10^{-3}	18.9
		67	2.6×10^{-3}	19.7
	DMAc	59	1.7×10^{-2}	13.0
		79	2.6×10^{-2}	47.0

exhibited the lowest oxygen permeability as it is not sulfonated, while Nafion® exhibited the highest oxygen permeability. To what extent this parameter, gas permeability, affects the overall performance of the cell is yet to be understood [8].

The catalyst activity and its relationship to the ionomer type and content are also often investigated. The effect of ionomer on transport losses, specifically oxygen transport, has been investigated in Refs. [35,37,38]. Sambandam et al. investigated the influence of the ionomer properties on oxygen permeability and ionomer-phase oxygen transport resistance. In Ref. [37], they measured the oxygen permeability through three polymers, Nafion®, s-PEEK and s-PSU using chronoamperometry in conjunction with an embedded cylindrical platinum microelectrode. They found that oxygen permeability through Nafion® is much higher in comparison to the other two polymers, which was attributed to the differences in microstructure of Nafion® and hydrocarbon-based polymers. The low permeability also correlated closely with a

Table 5
Degree of sulfonation, proton conductivity and water uptake of s-PEEK polymers in comparison to Nafion 117 [39].

	Sulfonated PEEK				Nafion 117
Sulfonation time (h)	6	9	12	24	
DS (%)	50	60	70	90	
Proton conductivity (S/cm)	1×10^{-2}	9×10^{-2}	1×10^{-1}	–	1.3×10^{-1}
Water uptake (%)	33.5	42.3	115.4	–	24.7

discrepancy arises from the difficulties associated with the technique. In particular, the challenges were associated to internal shorting within the sensing electrodes and hence the errors of this technique were too high.

As per the discussion above, it is clear that the measurement of the conductivity of the ionomer is challenging. In general, however, one can take the DOE targets for the protonic resistivity of the membrane as a basis for the design of new ionomer materials. The area specific proton resistance 2020 targets are dependent on the maximum operating temperature and water partial pressure and is given as 0.02 Ω cm^2 for 80 °C and is 0.2 Ω cm^2 for −20 °C [190].

The second parameter of interest when investigating the ionomer in the catalyst layer is its gas permeability. Permeability, in this context, is classified based on the solubility and diffusion of the gas, most importantly oxygen, within the ionomer. In general, it is believed that the diffusion of oxygen is faster in the hydrophilic domains of the ionomer, while its solubility in the hydrophobic regions is higher [48,49]. As seen in Tables 2–5, the oxygen permeability, and hence its solubility and diffusivity, is higher in PFSA ionomer than hydrocarbon ionomers. This was explained to be associated to the high oxygen solubility in the fluorous domains of PFSA ionomer [50]. The effect of ionomer type on the oxygen permeability; D_fC_f (product of the diffusion coefficient and oxygen concentration in the film), was investigated in Ref. [51]. Three types of polymers were studied; sulfonated polyimide (PIS), sulfonated polyetherketone (s-PEEK) and non-sulfonated poly-benzimididazole (PBI) as well as Nafion®. Not surprisingly, PBI

high transport resistance. This similar finding was also the focus of their work in Ref. [37], where they found that s-PEEK and s-PSU bound electrodes suffered from binder phase diffusion limitations as well as gas phase diffusion limitations. On the other hand, PFSA bound electrodes predominantly exhibited gas-phase diffusion limitations. A common observation is that much slower ORR kinetics are measured with the use of non-PFSA ionomers; hence, resulting in larger activation polarization losses in the cell's cathode. The origin of these losses is still to be fully understood, but adsorption processes and the morphology of the ionomer on the Pt/C surface are believed to be the dominating factors for these losses [8].

Estimation of the interfacial transport resistances within the catalyst layer are also of interest. In Ref. [52], Owejan et al. highlighted the local oxygen transport losses at the gas/ionomer interface to the Pt surface. They suggested that transport resistance through the ionomer coating is a function of both Pt surface area and the particle dispersion. Electrode design was suggested as a means of minimization/mitigation of oxygen transport losses. Pivovar and Kim used polarization curve and high frequency resistance data to quantify the interfacial resistance at the membrane/electrode interface [53]. The measured resistance varied from 8 to 57 mΩ cm^2, depending on the membrane type.

Wettability is another parameter that is of interest as a measure of the ionomer type. It is a measure of the water transport within the catalyst layer. The catalyst layer plays an important role in managing and controlling the overall water content within the cell

and the content can directly affect not only the proton conductivity of the ionomer but also its durability. Water content in the ionomer of the catalyst layer is linked to oxidation of carbon supports, chemical degradation of the ionomer as well as Pt dissolution [54]. A decrease in the water content can result in side chain scission, creating a large amount of weak end groups and accelerating degradation [54]. Wettability from a polymer science perspective is often studied in terms of water uptake of the polymer and in some sense is directly related to the ionic conductivity of the polymer. The intrinsic changes in the microstructure of the ionomer film lead to the change in its conductivity properties as has been measured in Refs. [40,41]. A decrease in the thickness of the polymer from micrometer-level to 100 nm leads to a decrease in its conductivity by an order of magnitude. In Ref. [54], it was also shown that the decrease in thickness leads to a decrease in the water uptake of the ionomer film; thus, suggesting that the thickness dependent water uptake becomes more influential at ~10 nm thick ionomer films in the CL [55]. Kusoglu investigated water uptake in the CL as a function of the relative humidity and compared it to the bulk membrane to shed some light onto the mechanisms controlling water transport through thin film ionomer [54]. The water content in the CL PFSA ionomer was found to be lower than in the bulk membrane (~one third of that of the membrane). The water uptake also improved in the presence of Pt, which was associated with the influence of the morphology of the ionomer within the layer. Investigating the time constants of water-vapor uptake, they suggested that water sorption into the ionomer thin film is not a purely diffusion controlled process, but rather another mechanism is dominant. They suggested that the mass transport is likely limited by the interfacial resistance due to a more hydrophobic surface and environment effects [56,57].

2.1. Alternative membranes to Nafion®

As chemical degradation of Nafion® is an issue in the catalyst layer and hydrocarbon polymers possess low permeability and ionic conductivity, alternative ionomers should be investigated. A detailed review of membranes for use in polymer electrolyte membrane fuel cells is given by Mehta and Cooper, where they identified 60 alternatives to Nafion® and categorized them into ill-suited and suitable, pending more research, for use in automotive PEM fuel cells [58]. They based their rejection of 46 of these materials on 13 reasons; namely, No FC Data (Conceptual), Expensive, Fire Risk, Low Durability, Poor Performance Property, Water Soluble, Shrinkage (low flexibility), Low Conductivity, Low Thermal Stability, Low Stability, Depolymerization, No Longer in Production. The possible alternatives to Nafion membranes are summarized below [58]:

i. α,β,β-Trifluorostyrene grafted membrane (partially fluorinated)
ii. Acid-doped polybenzimidazoles [PBI] membrane (non-fluorinated composite)
iii. BAM3G membrane (Ballard Advance Material of Third Generation Membrane) (non-fluorinated)
iv. Base-doped S-polybenzimidazoles membrane (non-fluorinated composite)
v. Bis (perfluoroalkylsulfonyl)imide membrane (perfluorinated)
vi. Crosslinked or noncrosslinked sulfonated poly-etheretherketone membrane (non-fluorinated)
vii. Gore-Select™ membrane (perfluorinated)
viii. Imidazole doped sulfonated polyetherketone [s-PEK] membrane (non-fluorinated)

ix. Methylbenzensulfonated polybenzimidazoles membrane (non-fluorinated)
x. Methylbenzensulfonate poly(p-phenylene terephthalamide) membrane (non-fluorinated)
xi. Perfluorocarboxylic acid membrane (perfluorinated)
xii. Poly(2-acrylamido-2-methylpropanesulfonic acid [poly-AMPS] membrane (Other)
xiii. Styrene grafted and sulfonated poly(vinylidene fluoride) membranes [PVDF-g-PSSA] (partially fluorinated)
xiv. Sulfonated naphthalenic polyimide (non-fluorinated)
xv. Sulfonated poly(4-phenoxybenzoyl-1, 4-phenylene) (s-PPBP) (non-fluorinated)
xvi. Supported composite membrane (other) − Composite membrane is made of ion conducting polymer (ICP) and poly-p-phenylene benzobisoxazole (PBO) substrates

Another type of membrane that has gained much interest lately is the short-side chain (SSC) and low equivalent weight PFSA. The short-side chain polymer was developed by Dow Chemicals [59,60], but its production was discontinued due to the high cost of its synthesis. However, its production was later commenced by Solvay Solexis under the commercial name of Hyflon Ion, which was then later changed to Aquivion™ and is often referred to as the short-side chain polymer in literature. Its chemical composition is given in Fig. 2. As seen from the figure, the feature of this SSC polymer is that it contains a shorter pendant side-chain that carries the functional ion-exchange group.

Comparisons between the two types of polymers (short- and long-side chains) reveals that SSC polymers possess a much higher crystallinity at given equivalent weight and a higher glass transition temperature, T_g, [62]. Hence, this membrane is promising for high temperature and low humidity operation of the fuel cell [63]. The enhanced crystallinity also allows for the decrease of the equivalent weight (EW) of the polymer without the risk of membrane dissolution or excessive swelling. In turn, a higher charge carrier concentration can be achieved, increasing the proton conductivity of the polymer [64]. Much work can be found in literature that discusses the use of this polymer as the bulk membrane in the cell; for instance [64–70]. In Ref. [67], short-side chain PFSA membranes with various IEC (IEC 1.30, 1.37, 1.43 and 1.50 meq g^{-1}) were investigated. Again, they found that under dry conditions SSC membranes show better performance as water transport rate is increased. Under the dry condition, inlet relative humidity of 30% and cell temperature of 110 °C, a 40% decrease in current was measured at 500 mV with the use of Nafion® ionomer in comparison to a SSC ionomer. They found that water permeation rates and the effective proton mobility are linked, but the increase in water content does not necessarily lead to an increase in water transport and effective proton mobility. The effect of equivalent weight of the membrane on the degradation of the cell was examined in Ref. [68].
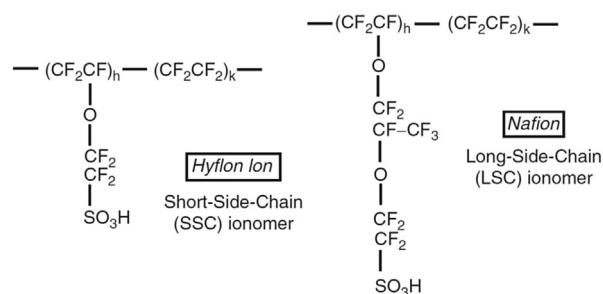

Fig. 2. Polymer structures of Hyflon Ion/Dow and Nafion *Reproduced from Ref.* [61] *with permission from Springer.*

The membranes under investigation were 750 EW SSC, 950 and 1100 EW LSC. 1100 EW LSC membrane showed the best performance and the 750 EW showed a better performance than the 950 EW; a cell voltage enhancement at 1.0 A cm^{-2} reached at 100 mV at 95 °C and 30% RH. The higher durability of the 750 EW over the 950 EW membranes was attributed to the shorter sulfonic acid side-chains present in the lower equivalent weight material. In ionomers with the same equivalent weight, those with shorter sulfonic acid side-chains have been shown to display higher durability due to decreased water swelling and absence of a tertiary carbon and lower concentration of ether linkages. The 1100 EW increased durability over the 950 EW is attributed to higher concentration of sulfonic acid groups in the latter. Using first principles based molecular modelling, the flexibility in both the backbone and side chains of PFSA membranes was demonstrated to be important to effectively transport protons under low humidity conditions [69].

Recently, there has also been an increasing interest in investigating the feasibility of using this polymer as the ionomer binder in the cathode catalyst layer [64,70–74]. The comparison carried out in Ref. [58], on SSC–Dow 840 and Dow 1150, demonstrated that the combination of a high IEC, high mechanical stability (e.g. by increasing crystallinity, molecular weight, cross-linkage or introducing interacting particles) results in an increase in proton conductivity and lower electroosmotic drag. The authors also anticipated the preservation of the morphology of the membrane/electrode interface at the same conditions where Nafion® 117 starts to show plastic deformation.

In general, two things must be taken into consideration when investigating new ionomer types for the catalyst layer; (i) its durability and stability and (ii) its compatibility with the bulk membrane [36,75,76]. The resistance of the MEA is affected by the "connectedness" of the catalyst layer and the membrane; specifically the ionomer and the membrane. Delamination of catalyst layers prepared with Nafion® ionomer from s-PEEK membranes was observed in Ref. [77] after some operational hours; hence, affecting the long-term stability of the cell. On the other side, the use of s-PEEK polymer as the ionomer in the catalyst layer and as the electrolyte membrane showed enhanced adhesion between the CL and membrane.

3. The solvent

Just as its literal definition suggests, the solvent is used in the ink of conventional catalyst layers to dissolve the dry components and form a uniform solution. The choice of the solvent often depends on the preparation method of the ink and its subsequent dispersion method on either the gas diffusion layer or the electrolyte membrane. For instance, roll to roll coating usually requires viscous inks with high solids content (>5 wt%) and high boiling point additives; whereas spray coating requires low solids content (<2 wt%) and faster evaporating alcohol- or water-based solvents [8]. Some of the solvents used in literature along with the deposition method are summarized in Table 6.

The choice of the solvent does not only dictate the deposition method and its drying properties, it can also affect the overall durability of the catalyst layer as reported in Ref. [82]. In Ref. [82], Kim et al. that the choice of solvent has a direct effect on the agglomeration of the carbon particles and hence on the overall durability of the catalyst layer. They investigated three types of solvents, N-Methyl-2 pyrrolidone, Glycerol, and water based additives, and their effects on the stability of the cell's performance [82]. Despite significant changes in the measured ECSA of the three electrodes, they found that this is not indicative of the stability of the electrodes. Their findings are summarized in Fig. 3. They

attributed these differences in performance to the structural differences, specifically of the ionomer, within the catalyst layer. Small angle neutron scattering investigation of ionomer films prepared with water based additive, NMP and glycerol revealed a higher aggregation of the ionomer prepared with a water based additive [83]. This aggregation implies lower mechanical properties of the ionomer. Measurements of stress/strain of casted Nafion films prepared with water based solvent, NMP and glycerol showed that mechanical properties of ionomer films prepared with water based solvent are indeed much lower than those of ionomer films prepared with NMP and glycerol solvents. The implications of the two studies in Refs. [82,83] are of great importance for the design of next generation electrodes. The observations imply that the cell performance is largely governed by the catalyst-polymer-solvent interactions that directly affect the catalyst-void-ionomer (three-phase) interfaces rather than simply the ECSA of the Pt catalyst. Similar works on the effect of solvent on the catalyst layer performance with Nafion® as the ionomer were carried out in Refs. [84,85]. Again, in both studies, catalyst layers prepared with a water based solvent showed lower performance. In Ref. [84], Huang et al. investigated the use of 5 different dispersion media. With the use of methanol and water as the solvent, the catalyst was not as well dispersed in the solvent and cracks eventually formed upon drying. The effect of the dispersion medium on the high frequency resistance, in other words the proton conductivity, was attributed to the interaction between the ionomer microstructure/network and the solvent [85]. In Ref. [86], the authors investigated the use of glycerol as a solvent and its effect on the micro structure of the catalyst layer. They found that the amount of glycerol affects the pore volume of the catalyst layer. If glycerol is not fully removed from the catalyst layer, it can block the primary and secondary pores and hence hinder the transport within the layer. Removal of glycerol by steam water is advised.

The choice of casting solvent and its effect on the conductivity of SPEEK polymers was investigated in Ref. [38]. Two solvents, N,N-dimethylacetamide (DMAc) and water-acetone mixture (DMF) were investigated. They demonstrated that the conductivity of the polymer depends on the casting solvent as well as its degree of sulfonation. DMF was shown to enter in strong hydrogen bonding with sulfonic acid groups of s-PEEK; reducing the number of protons available for charge transfer and hence the conductivity of the polymer. A conductivity decrease was also suggested due to the interaction between DMF and DMAc with residual sulphuric acid during high temperature treatment. With this interaction, dimethylaminium sulphate and corresponding carboxylic acids are formed.

4. The support

Conventionally, the most commonly employed support in the catalyst layer of PEM fuel cells is carbon; mainly due to its low cost, chemical stability, high surface area and affinity for supporting metallic nanoparticles (i.e. the catalyst). Specifically, carbon black and graphitized carbon are typically used and their specific area ranges from <10 to >2000 m^2 g^{-1} [87]. With its tendency to aggregate, carbon blacks form agglomerates of carbon particles exhibiting a bimodal pore size distribution. Typically, the bimodal distribution includes 2–20 nm sized pores within agglomerates of carbon particles and larger >20 nm sized pores that exist between aggregates of agglomerates. These two distinct regions are often referred to as primary and secondary pores, respectively [4,88] and are illustrated in Fig. 4(a).

Ketjen Black and Vulcan XC-72 are commonly used carbons as the catalyst support in PEM fuel cells. Their use has been investigated in Refs. [24,43]. Ketjen Black exhibits high surface area,

Table 6
Types of solvents used in literature.

Solvent	Deposition method	Reference
Water/methanol mixture (1:1)	Spray deposition	[24]
Glycerol/ethanol mixture	Spray deposition	[78]
Ethanol/isopropanol mixture	Brushing deposition	[26]
Isopropyl alcohol	Brushing deposition	[25,27]
Water	Not specified	[79][a]
Glycerol and methanol	Brushing deposition on a decal	[34][b]
Isopropyl alcohol	Spraying directly on the electrolyte membrane	[80]
Isopropyl alcohol and deionized water	Coating on a decal	[81]

[a] The authors suggested that cold Nafion® solution is used to avoid catalyst burning upon the addition of the catalyst. They also suggested that to prevent catalyst burning, the catalyst on its support should be first wetted by a small amount of water [79].

[b] The electrode was prepared using the decal transfer method to the electrolyte membrane. Two solvents were used for a two step deposition on the decal. Glycerol was used to mix the carbon-supported catalyst, which was then brushed onto the decal. The Nafion® solution was mixed in methanol, with this mixture then brushed onto the catalyst/carbon already brushed on the decal. This two way brushing deposition was used to vary the amount of ionomer within the final catalyst layer [34].

890 m^2/g, while Vulcan XC-72 is a low surface area material, 228 m^2/g. In Ref. [24], Soboleva et al. investigated the microstructure of both supports, the platinum/carbon catalyst powders and the three-component (platinum/carbon/ionomer) catalyst layers. They found that the overall structure of the three-component catalyst layer is highly dependent on the carbon support. Ketjen Black was found to possess a significant fraction of micro-pores, 25% of the total pore volume, which contributed to the distribution of the Pt on the support. The deposition of Pt on Ketjen Black was found to occur at the mouth of the support's micro-pores, decreasing the total surface area. However, this trend was not measured in the case of Vulcan XC-72 as shown in Fig. 4(b) and (c). The addition of ionomer to both Pt/carbon catalyst powders significantly reduced the total surface area; however, the overall trend of the pore size distribution did not vary with the addition of more solid material. In their following work, the group correlated the performance of the cell to the microstructure of the catalyst layer [43]. Investigation of the water uptake revealed that a broad pore size distribution in the catalyst layer enhances water retention, whereas narrower meso-porous pore size distribution enhances water repelling action. To further understanding in regards to the optimum ionomer content within the catalyst layer, they investigated various ionomer contents and compared it to the standard 30 wt% ionomer MEA. The relationship between the optimum ionomer content and the carbon supported was attributed to the pore size distribution of the carbon and hence the resultant distribution of the ionomer within the pores of this particular support. They suggested that an optimum ionomer content is a function of surface area of pores larger than 20 nm. Higher ionomer content is required to create a continuous proton conducting network in the case of a higher meso-porous surface area. Similar findings were reported in Ref. [89]. Liu and co-workers concluded that the difference in surface area and pore volume between the two carbons stems from pores smaller than 4 nm. They suggested that although ionomer penetrates into these small pores, it does not contribute to the electrode's proton conductivity. If the total electrode ionomer/carbon ratio is corrected to the amount of ionomer in the primary pores, the dependency of proton resistivity of both carbons on the effective ionomer/carbon ratio is identical. From their work, they concluded that "(1) carbon supports with higher surface areas require more ionomer in order to achieve the same proton conductivity. (2) For the same Pt loading, carbon supports with higher surface area tend to give smaller Pt particles and better Pt dispersion [90], resulting in higher Pt areas and consequently lower ORR overpotential, given similar area specific activity."

Although carbon is the most widely used in the conventional design of a catalyst layer, its durability still raises a major limitation to the commercialization of PEM fuel cells. This is especially linked to the serious corrosion of carbon due to surface oxidation and carbon dioxide evolution in the PEM fuel cell environment [91,92]. Due to the oxidation process, catalyst detachment from the support and accelerated coalescence of catalyst nanoparticles on the support are encountered; hence, reducing catalyst activity [93]. Investigation of the interaction between the catalyst and the carbon support is hence of interest in order to reduce its detachment or avoid it all together. A method to increase the dispersion of the metal crystallites and their bond to the carbon support is functionalization. In general, functional groups predominate in the graphene layer of carbon black supports; most commonly oxygen, nitrogen and sulfur-based. For instance, significant amount of sulfur moieties were found in popular carbon black supports, such as Vulcan XC-72 [94]. Swider and Rolison found up to 5000 ppm of sulfur (by weight), corresponding to 3.3 S per Pt, which would be enough to poison all electrocatalyst present. In their study, however, they found that once water, heat and strong physical contact between Pt and carbon are all present, Pt catalytically oxidizes some of the covalent sulfur in the Vulcan carbon. The remaining unoxidized sulfur is zero-valent and appeared to not be initially in contact with the Pt. However, it could become a source of poisoning to the Pt with long-term electrochemical use. Unlike sulfur, oxygen and nitrogen functional groups are used to aid the electrocatalysis on the dispersed metal crystallites. In Ref. [94], oxygenated carbon functional groups (e.g. COOH, −OH) were shown to decrease the Pt metal surface area by promoting increased crystallite size. Similar findings were reported for nitrogen functional groups in Ref. [95]. Roy et al. reported enhanced oxygen reduction activities on electrodes functionalized with nitrogen in comparison to untreated carbon. They suggested that during catalyzation, the platinum may bind more strongly to pyridinic sites; hence, preventing Pt particles from sintering. The increased electron donation from pyridinic nitrogen functionality to Pt was given as a probable reason for the enhanced ORR activity.

Taking into consideration that the interaction between the catalyst and support is of high importance in the optimization of the catalyst design, much work is dedicated in the literature to finding alternative supports to the conventional carbon powders. In the following sections, we summarize some of the efforts.

4.1. Boron-doped diamond (BDD) powder

In literature, BDD electrodes have been researched as alternative to the conventional carbon electrode for the anode of direct methanol and ethanol fuel cells [96–100]. This is mainly due to the excellent properties, which BDD possesses as a catalyst support, mainly long-term thermal stability, extreme chemical stability and
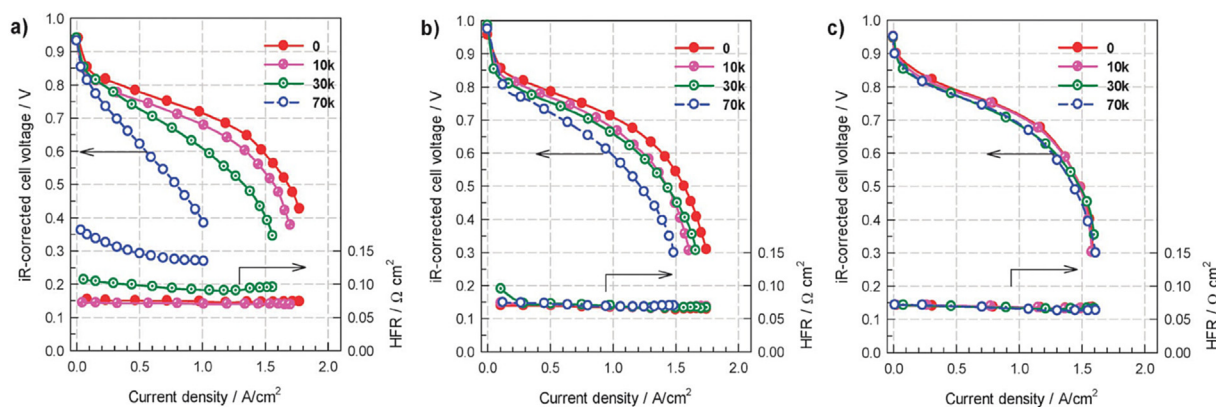
(A)
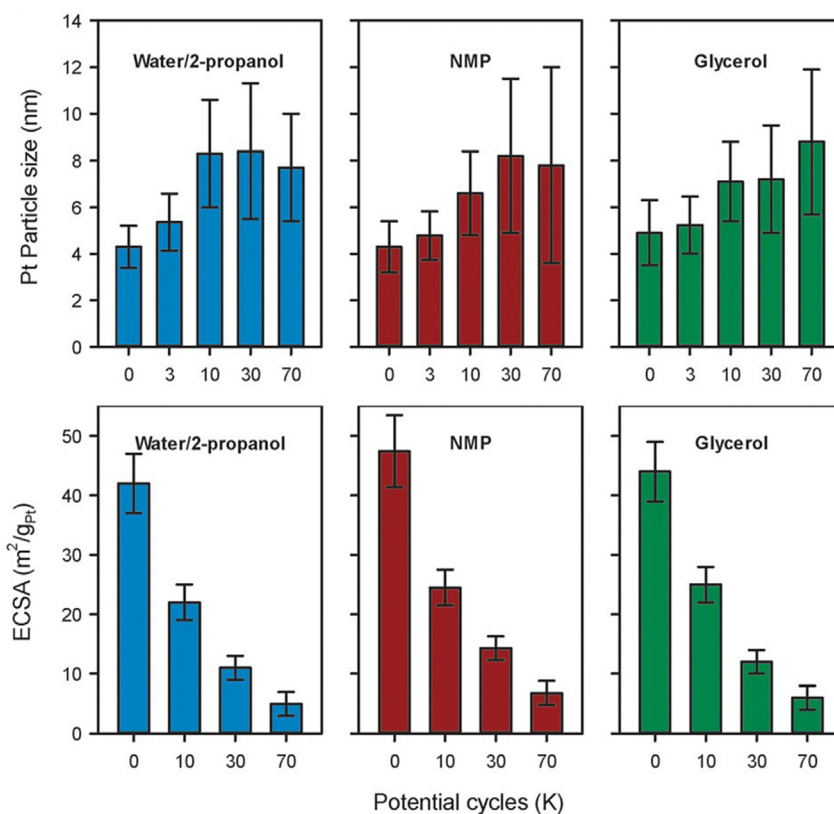
(B)

Fig. 3. Long term effect of solvent, *N*-Methyl-2 pyrrolidone, Glycerol, and water based additives, after potential cycling on (a) the performance of the cell; and (b) Pt particle size and the electrochemical active surface area of the catalyst layer *Reproduced from Ref.* [82] *with permission from the PCCP Owner Societies.*

corrosion resistance in a hostile environment [101,102]. The electrical conductivity of BDD polycrystalline films obtained by chemical vapor deposition has been reported to be 100 S cm^{-1} [103]. Various deposition methods of the catalyst to the surface of the BDD exist, such as sol-gel [104], microemulsion [96], electrodeposition [105] and electroless deposition [106]. The deposition method directly affects the distribution and ultimately agglomeration of the catalyst on the surface and hence the interaction with the surface of the support. In Ref. [105], two methods for the deposition of Pt particles on the BDD surfaces were evaluated; chemical deposition and electrochemical deposition. Electrodes prepared via chemical deposition showed irregular distribution of platinum clusters on the diamond surface as well as the formation

of agglomerates of Pt particles. The agglomeration was related to the inhomogeneity of the interfacial surface tension of the BDD support as well as sintering of the particles during the thermal treatment. With this method, it was found that dissolution/detachment of the Pt during potential cycling is enhanced and was attributed to the weak binding energy between the Pt adatoms and the BDD support in comparison to the binding energy between the Pt adatoms themselves; hence favoring 3D Pt crystal growth [107]. In general, some of the issues that can arise in the preparation of this type of catalyst layers are stability of the catalyst due poor adhesion, inability to control the particle size and distribution and insufficient uniformity in the deposition of the catalyst [106].

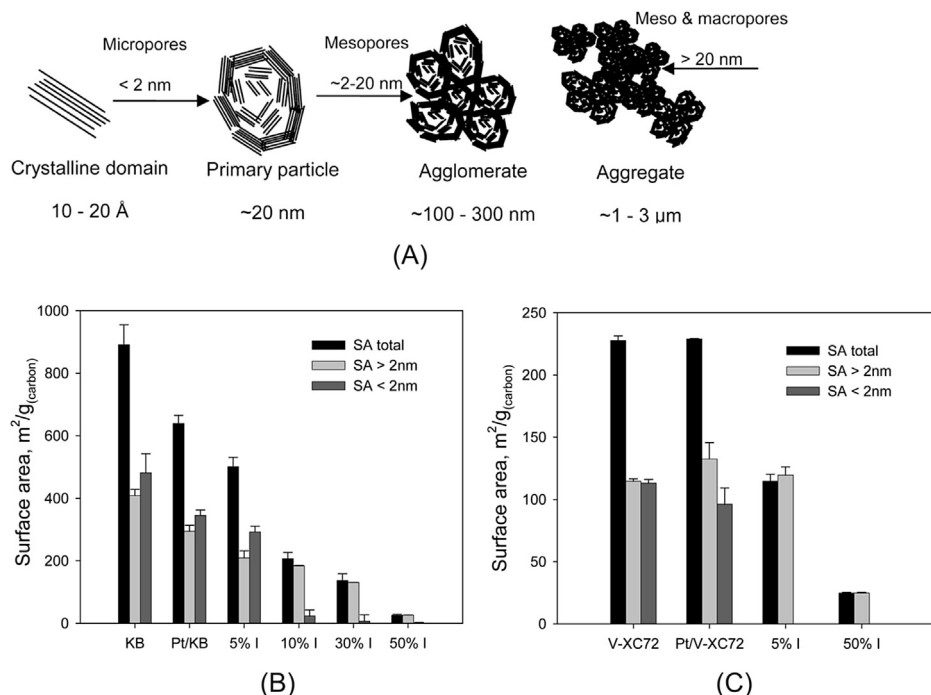The use of BDD as support in PEM fuel cells is of rising interest;

Fig. 4. (a) Schematic representation of the microstructures of carbon black supports: turbostratic crystalline domain, primary carbon particle, agglomerate, and aggregate of agglomerates. Representative micro-, meso-, and macropores are indicated by arrows; Surface areas of Ketjen Black, Pt/C, and the corresponding catalyst layers showing the effect of platinum and ionomer loading on the detectable SA of the examined systems (b) Ketjen Black used as the carbon support; (c) Vulcan XC-72 used as the carbon support *Reproduced from Ref.* [24] *with permission from the American Chemical Society.*

thus, investigating its durability in-situ is of importance. In Ref. [108], the durability of a BDD electrode was investigated in-situ and compared against that of a conventionally supported catalyst layer (Vulcan XC-72) and a multi-walled carbon nanotubes electrode. With accelerated stress tests, the BDD supports showed improved durability over their counterpart electrodes. This was mainly attributed to the unchanged nature of the surface of the BDD electrode; hence, reducing Pt detachment in this type of electrode.

4.2. Nanotubes and nanofibers

Carbon nanofibers (CNFs) are produced via catalytic conversion of carbon containing gases and have a diameter range of 3–100 nm and length between 0.1 and 1000 μm [109]. The microstructure of these fibers, specifically their shape, size, and surface area can be controlled by the catalyst composition and reaction conditions [110] and their surface chemistry can be modified using chemical functionalization treatments [111]. Functional groups containing oxygen were shown to decrease the electronic conductivity of CNFs from 2 to 3.5 S cm^{-1} to 0.20–1 S cm^{-1} when surface oxygen content increased from 1.5 wt% to 5 wt%. Further oxidation can eventually destroy the original fibrous structure [112]. The use of hydrogen as a surface functional group was also shown to affect the electrical conductivity of CNFs in Ref. [110] where the maximum conductivity of around 2.75 S cm^{-1} was found for 10% H$_2$. Carbon nanofibers are classified into three types (i) ribbon-like CNF, (ii) platelet CNF and (iii) herringbone (or stacked-up) depending on the orientation of the nanofibers with respect to the growth axis. Interest in these catalyst supports for use in fuel cells arises due to the need to reduce platinum content in the cathode catalyst layer, while increasing its catalytic activity. In this case, this is achieved by surface tailoring of the support resulting in high and uniform concentration of supported Pt particles with a size of 2–3 nm;

hence smaller thickness of the cathode catalyst layer is also attained [113]. The use of carbon nanofibers as the catalyst support for PEM fuel cells has been extensively researched in the literature, where studies are mainly focused on the synthesis method as well as the functionalization treatments [113–118]. The growth mechanism also has an effect on the characteristics of the fibers. For instance, Herringbone CNFs have intermediate characteristics between parallel and platelet types; hence, exhibiting higher catalytic activity than the parallel and better durability than the platelet forms [119].

Carbon nanotubes (CNTs) are two dimensional structures with the tubes formed by rolled up single sheets of hexagonally arranged carbon atoms. This type of support is classified into single walled (SWCNT) and multi-walled (MWCNT) with SWCNTs providing larger surface area and MWNTs being more conductive. Carbon nanotubes are well documented in the literature as catalyst supports for PEM and direct methanol fuel cells [120–125]. The main difference between carbon nanofibers and carbon nanotubes is their alignment and hence potential catalyst anchoring sites. This in turn determines the activity of the catalyst and the overall performance of the cell. In literature, carbon nanofiber-supported catalysts have shown a better performance than their nanotubes counterparts [126–128].

4.3. Conducting polymers (CPs)

Interest in replacing the traditional carbon support with a conducting polymer arises from the need to reduce corrosion of the support and ultimately catalyst activity loss. Conducting polymers possess high accessible surface area, low resistance and high stability [129]. Electric charge easily flows through the polymer matrix and is even more enhanced with the use of porous conducting polymers [129]. The porous structure of CPs allows for the increase of the specific area of the active surface and increases the tolerance

of the polymer-supported Pt particles to CO poisoning [129]. Another advantage for this support is the elimination of the Nafion® ionomer in the catalyst layer as these conducting polymers are not only electron conductors but also proton conductors. Various studies have been carried out to investigate oxygen reduction [130—134] and hydrogen oxidation [133,135] on conducting polymer coated electrodes. In Ref. [136], the authors reported the use of Polypyrrole/polystyrene sulphonate composite (PPY/PSS) as a catalyst support in the cathode of a PEM fuel cell, where they suggested optimization is needed. They reported an initial electronic conductivity of 3 S cm^{-1} of the PPY/PPS composite that decreases to 0.3 S cm^{-1} upon Pt deposition [136]. Ongoing research is still carried out to fully understand the use of this support in the catalyst of PEM fuel cells and consequently optimizing its design and stability [137—140].

4.4. Other supports

Other types of supports include multi-layer graphene and reduced graphene oxide [141—147] as well as metal nitrides, carbides and oxides [148—153]. A detailed review of various supports used in direct methanol and polymer electrolyte fuel cells is given in Ref. [154].

4.5. 3 M's nano-structured thin film catalyst layers

Nano-structured thin film catalyst layers are composed of catalyst-coated whiskers as shown earlier in Fig. 1(b), which comprises the primary differentiating feature to conventional catalyst layers. These whiskers act as the support to the catalyst metal, e.g. Pt. In the case of the 3 M NSTF, the catalyst layer contains neither carbon nor additional ionomer in the catalyst layer; making them 20—30 times thinner than conventional Pt/C based MEA's [11]. The material used to manufacture the whiskers is an organic pigment known as perylene red (PR) [11] and they are highly inert thermally, chemically and electrochemically [155] and non-conductive to electrons. Much work has been carried out by Debe et al. to elucidate the differences between these catalyst layers and their conventional counterparts [11,21,155—159]. In their recent publication, they suggested that there are four primary differentiating characteristics of the 3 M NSTF catalyst layers [159].

  i. **Nature of the support particle**—The support used in the NSTF is a pure, organic molecular solid in the form of a crystalline whisker. The perylene compound used in these catalyst layers is electrochemically stable to RHE potentials above 2 V. Hence, unlike their conventional counterparts, NSFT catalyst layers do not undergo any electrochemical corrosion under operating fuel cell conditions. The high aspect ratio (length to width) of the whiskers and the areal number density results in a large Pt surface area.
 ii. **Nature of the catalyst structure**—The polycrystalline thin film nature of the structure results in a specific activity for the oxygen reduction to be 5 to 10 times higher than for conventional catalyst layers. Further, the catalyst is highly agglomerated and is hence less susceptible to loss of surface area by agglomeration.
iii. **Nature of the process**—The preparation technique of these catalyst layers assures the generation of the whiskers forming a perfect, oriented monolayer. The process is vacuum based roll to roll coating; hence, allowing for high production.
 iv. **Nature of the electrode**—The electrode is 20—30 times thinner than the conventional MEA's. This is mainly due to the absence of carbon black. Hence, in the absence of the

carbon black, the electrical conductivity is provided by the polycrystalline catalyst thin film itself. Whisker to whisker contact is established once the catalyst layer is transferred to the membrane. Additional ionomer is also not required. Studies by both 3 M and GM showed that adding ionomer to the NSTF resulted in increased mass transport impedance to the catalyst surface [160]. The extreme thinness of the electrode implies that oxygen mass transport impedance is minimized at standard operating temperatures. Hence, at higher current densities, 100% utilization of the catalyst is possible. With the catalyst coated whiskers being partially embedded in the PEM surface, the proton pathway from the catalyst surface to the membrane ionomer is very short, and thus, resistance to proton transport is also low. However, due to absence of ionomer within the catalyst layer, there is still debate in regards to the mechanisms of proton conduction. According to Debe, proton conduction occurs through hydronium ions moving over the Pt surface typically covered with hydroxyl species [159]. This is especially significant with adequate humidification. Chan and Eikerling [161] proposed that electrostatic interaction between Pt surface and the protons could provide path for proton conduction. In Ref. [162], Sinha et al. stated that electrostatic interactions are unlikely to be the predominant mechanism of proton conduction as the NSTF electrode is free of bulk liquid water under low relative humidity conditions. Instead, they suggested that dependency of proton conduction on the relative humidity might be due to different amount of water adsorption on Pt surface. Under these low humidity levels, they also hypothesized that the reaction takes place at the membrane/NSTF interface; see Fig. 5. This implies that much of the proton conduction, under these conditions, occurs through the PEM. In any case, the consensus, between all these studies, is that more work is needed to elucidate the mechanism of proton conduction in ionomer free catalyst layers.

As mechanical and chemical stability of the 3 M NSTF is one of their major "selling" points, Much work has been carried out by Debe et al.; see Refs. [11,21,155—159], to investigate the long term durability of these catalyst layers. At OCV of >0.90 V under H$_2$/air and an OCV of ~1.23 V under air/air in start-up/shut-down modes,
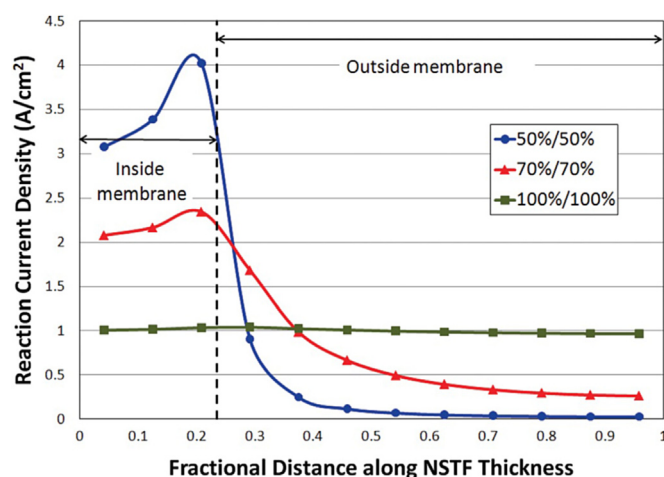

Fig. 5. Reaction current density distribution in NSTF electrode for an average current density of 1.0 A/cm^2 for H$_2$/O$_2$ operation at various channel RH values, 150 kPa$_{abs}$ channel pressure and 80 °C cell temperature *Reproduced from Ref.* [162] *with permission from the Electrochemical Society.*

local fuel starvation and oxygen cross-over can occur. At these conditions, loss of Pt through Pt dissolution and agglomeration can occur due to oxidation of the carbon support; hence, the active surface area is reduced. Keeping this in mind, Debe et al. carried out a detailed investigation of the stability of NSTF catalyst layers under high voltage [21]. They showed that NSTF-Pt catalyst (0.15 mgPt cm^{-2}) are much more resistant to loss of surface area from high voltage cycling than are Pt/C (Ketjen Black) with 0.4 mgPt cm^{-2} loading. They calculated the activation energy for the surface area loss to be twice as high for the NSTF; implying that surface area loss rate is much slower for NSTF. This surface area loss was attributed to the agglomeration of Pt. They explained that the stability of the NSTF catalyst layers is very likely due to their thin film nature as well as the initial larger Pt grain size. They explained that NSTF-Pt grains are already highly or even fully agglomerated as they are contiguous and form a conformal layer covering the whisker core. This is not the case in terms of conventional catalyst layers, where Pt atoms are not fully in contact to each other and hence can diffuse away from their parent Pt particle and become inactive.

Comparing the cyclic voltammograms of the NSTF-Pt based MEA's and Pt/C based MEA's, Debe et al. found that the peaks of the CV of Pt/C based MEA's shifts as the MEA is aged as shown in Fig. 6. The shift occurs in the region of hydrogen desorption and Pt oxide formation. They pointed out that on Pt/C, the characteristic peak positions shift to become equal to those of the NSTF-Pt. They suggested that the peak positions are closely tied to particle size, with the size of the Pt/C crystallites approaching those of the NSTF catalysts. They also pointed out the new peak in the double layer region of the Pt/C CVs, which is consistent with the additional carbon

Fig. 6. Comparison of the initial (top) and final (bottom) full range cyclic voltammograms from the NSTF-Pt based MEAs and Pt/C based MEAs, showing shifts in peak positions and double layer capacitance occurring as surface area was lost. Note the change in the current density range for Pt/C between initial and final CVs *Reproduced from Ref.* [15] *with permission from Elsevier.*

oxidation (around 0.60 V). Similar trends were reported by Hasché and co-workers [163]. They investigated the durability of both MWCNT and conventional Pt/C catalyst layers via potential cycling (0.5–1.0 V vs. RHE for 10,000 cycles and 0.5–1.5 V vs. RHE for 2000 cycles). The findings of the study indicate that Pt particle growth of a Pt/C is controlled by Pt dissolution/re-deposition. A critical Pt diameter is reached after which the particle growth becomes negligible. The use of MWCNT as the support was not found to be detrimental to the Pt mass or its specific ORR activity in comparison to a conventional carbon support. However, durability was enhanced with the use of MWCNT, which was attributed to enhanced adhesion between Pt atoms and the graphene tube walls. Based on their results, they suggested that ECSA loss is mainly controlled by carbon corrosion associated with Pt particle detachment and loss of electrical contact.

Although the performance of the cell and its durability/stability have been shown to significantly increase with the use of NSTF-Pt based MEA's, some technical issues still face NSTF based MEA's. The major such issue is the propensity of the catalyst layer to flood under cool, wet operating conditions, which can result in negative effects under transient load operation. To investigate the NSTF transients under such conditions, Kongkanand and Sinha [164] developed a non-isothermal model taking into consideration water transport dynamics during current up-transients. This model complements their experimental work, where they showed that during such transients failure of the cell is inevitable upon cell reversal. They suggested that the thinness of the NSTF catalyst layer does not allow sufficient time for water removal and yields cell voltages at or below zero. They suggested that water management of these layers can be achieved with "(1) increasing the cathode water storage capacity governed by its thickness and porosity; (2) decreasing membrane thickness; (3) decreasing the water content in the membrane prior to the transient; (4) strengthening water removal to the channel by lowering the channel RH or by altering diffusion media water vapor removal properties". In Ref. [14], Debe suggested that water management through such thin catalyst layer can be achieved by forcing water removal through the anode rather than the cathode. He listed 5 factors to consider "(1) minimize amount of liquid water exiting the cathode; (2) use thinner membranes; (3) utilize natural hydrophilicity of NSTF catalyst; (4) use cathode-to-anode overpressure with $P_{H2} < P_{O2}$; (5) optimize anode GDL properties". Optimization of the anode gas diffusion layer backing and microporous layer coatings and their effects on the performance of ultra-thin electrode PEM fuel cells is the subject of study in Ref. [165].

5. The catalyst

Platinum is the catalyst of choice in fuel cells, and specifically PEM fuel cells, due to its proven high activity and stability under various operation conditions. Nonetheless, efforts are still needed to decrease the loading of Pt and essentially increase its dispersion within the catalyst layer without hindering its activity or durability. This is especially crucial on the cathode. On the anode, low loadings of Pt are sufficient for the activity of the layer and its durability. However, it is common to use Pt-metal alloy catalysts in the anode to reduce any contamination effects from the fuel feed. For instance, platinum is used in combination with less noble elements, such as Ru, Sn, Co, Cr, Fe, Ni, Pd and others to mitigate the effects of contaminants such as carbon monoxide and hydrogen sulfide [166–176].

The need for an alternative catalyst for the oxygen reduction reaction, which is highly active and stable, is the main driver for much of the work tailored towards the commercialization of PEM fuel cells. The two basic properties of the electrocatalyst
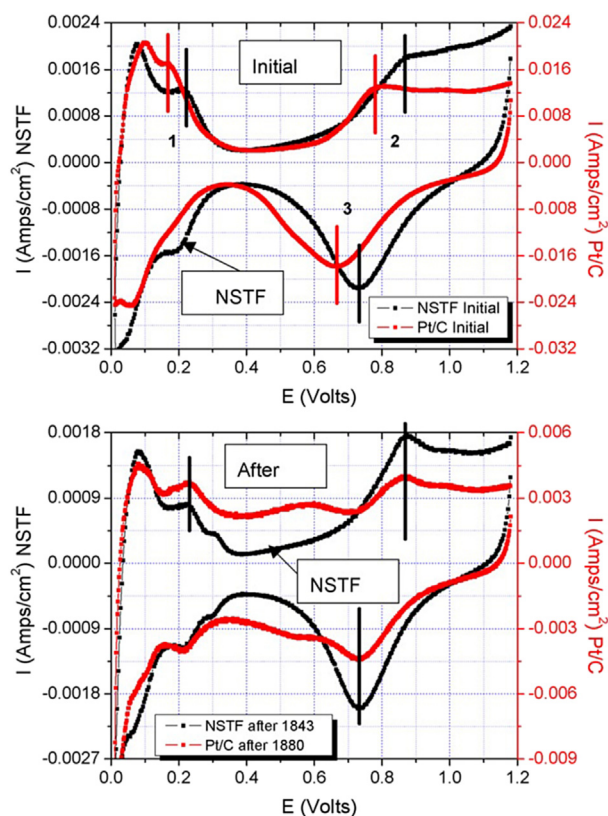
determining the rate of an electrochemical reaction are its electronic and geometric characteristics [177]. The surface structure of platinum can affect the bonding energy between the oxygen atoms and the Pt surface. In the extreme case, this can imply that neither adsorption nor chemisorption of oxygen will take place; hence, diminishing the activity [177]. The electronic properties of Pt are also closely linked to its geometric characteristics. In general, defects (e.g. steps or kinks) in the particle structure will alter electronic bonding of the atoms in the particle. Evidence from X-ray absorption spectroscopy (XAS) investigation of an operating cell indicates the dynamic response of the catalyst structure to the electrochemical condition [178]. Specifically, gradual increase of the structural order of Pt and contraction of the Pt−Pt distance upon decreasing the cell potential were recorded [178]. This correlates well with the theoretical calculations in Ref. [179], where the local atomic disorder in the catalyst was found to influence the oxygen reduction reaction. Electrons spin resonance (ESR) and XPS studies have also been used to highlight the electronic interaction and synergistic effects between catalyst and support. In Ref. [180], ESR was used to demonstrate the electron donation by Pt to carbon support, which was supported by XPS studies [181]. XPS illustrated that the metal acts as an electron donor to the support with the interaction dependent on their respective Fermi levels. Particle size and structural effects on the electrocatalysis of Pt have also been the focus of numerous studies with contradicting findings. Investigations by Zeliger [182] and Bett et al. [183] showed that the specific activity of oxygen reduction is independent of the Pt particle size. This, however, was in contradiction to the findings of Blurton et al. [184] and Bregoli [185], where in both studies a decrease in the particle size was found to decrease the specific activity of oxygen reduction. Origins of the different conclusions between these studies were later elucidated in Ref. [186]. Peuckert and co-workers measured the activity of a series of four catalysts with 5, 10, 20 and 30 wt% Pt, corresponding to a mean Pt crystallite sizes of 1, 1.1, 1.4 and 4.1, respectively. A constant activity for Pt particle sizes above 4 nm was measured and a decrease by a factor of 20 in the activity was obtained once the particle size decreased from 3 to 1 nm; suggesting an optimum particle size range for use in fuel cell cathodes. This finding only highlights the requirement for establishing the various dioxygen adsorption geometries on these highly dispersed electrocatalysts and also to establish a definitive oxygen reduction reaction mechanism [187].

Such effects are also evident in the change in the catalyst activity upon the alloying of Pt with another metal, where the structure of the catalyst changes. Activities of various catalysts researched and used in PEM fuel cells, such as commercial Pt/C, de-alloyed Pt_xCu_y/C and Pt_xCo_y/C, heat treated Pt_3Co/C and NSTF alloy, and have been summarized in Ref. [188]. One of the main messages to be taken from Debe's summary is that activities measured under the RDE environment and those measured in situ in the cell vary [188]. This, hence, reflects the complex environment of the catalyst in a working fuel cell and the difference of the "cleanliness" of the catalyst surface in RDE measurements (clean) and MEA (oxidized) [188]. The DOE targets for 2020 are based on mass activity measurements in an MEA environment run according to the experimental method detailed in Ref. [189]. The mass activity for pure platinum catalyst of 0.44 A mg^{-1}_{pt} @ 900 $mV_{iR-free}$ is set as the target for 2020 for transportation applications [190]. Whereas, the target for non-PGM catalyst activity per volume of supported catalyst is indicated as 300 A/cm^3 @ 800 $mV_{iR-free}$ [190]. Much work has been done in literature where the mass activity and the respective specific surface activity of various catalysts have been measured. For de-alloyed $PtCo_3$/C, the mass activity and the specific surface activity were reported in the range of 0.28 ± 0.05 to 0.38 ± 0.05 A mg^{-1}_{pt} and 701 ± 68 to 811 ± 99 μA cm$^{-2}_{pt}$,

respectively [191]. In the same study, the mass activity of de-alloyed $PtCu_3$ was measured as 0.41 ± 0.09 A mg^{-1}_{pt} and its specific surface activity as 873 ± 167 μA cm$^{-2}_{pt}$, while the mass activity of conventional Pt/C was reported as 0.13 ± 0.01 A mg^{-1}_{pt} and its specific surface activity as 179 ± 4 μA cm$^{-2}_{pt}$. Activities of Pt−Cu alloys were also reported in Ref. [192]. Mass activities in the range of 0.23−0.56 A mg^{-1}_{pt}, corresponding to a specific surface activities of 422.28−762.62 μA cm$^{-2}_{pt}$ were reported depending on the treatment of the alloy. The mass activity of carbon supported binary PtM_3 (M = Co, Ni, Cu) was reported as 0.346, 0.275 and 0.340 A mg^{-1}_{pt}, respectively, corresponding to a specific activity of 491, 248 and 472 μA cm$^{-2}_{pt}$, respectively [193]. These activities were compared to that of pure Pt, which was reported as 0.104 A mg^{-1}_{pt} and 166 μA cm$^{-2}_{pt}$. Values for the mass activity of pure Pt catalyst were reported in the range of 0.064−0.16 A mg^{-1}_{pt} depending on the carbon support and the content of Pt. The specific activity, hence, varied between 170 and 210 μA cm$^{-2}_{pt}$ [189].

The dependence of the ORR kinetics in an operating PEM fuel cell on the relative humidity has been investigated in Ref. [194]. It was shown that the kinetics are independent of RH at values above 50−60%, while an RH of 30% amounted to a 20 mV loss. This was attributed to the lowering of the proton activity via hydration. Experimental guidelines to measure the true ORR kinetics in an operating PEM fuel cell were set by the same group in Ref. [195], where the catalyst utilization is kept above 90%. The proton activity was also stated as a reason for reduced ORR activity at sub-zero temperatures [196]. In Ref. [196], Thompson et al. measured the ORR kinetics under subfreezing conditions where they found that the rate of oxide formation decreases at subfreezing temperatures. The linear behavior of the Arrhenius plots of current density at a constant was suggested to indicate that there is no fundamental change in reaction mechanism at subfreezing temperatures [196].

Despite a high activity measured for various catalysts, they are not yet practical for commercial use as they cannot satisfy all the electrocatalyst requirements for high current density and durability at low loadings. The major drawback of Pt-alloy catalysts is leaching of ions from the less noble metal. This leaching can lead to various ramifications; mainly, reduction of the membrane conductivity, increase in resistance of the catalyst layer due to increased ionomer resistance, lower diffusion of oxygen in the ionomer, degradation of the electrolyte membrane in the presence of cations such as iron and titanium [189]. Leaching of the non-noble metal can occur due to (i) excess base-metal deposited onto the carbon support during preparation, (ii) incomplete alloying of the base element to Pt due to a low alloying temperature, (iii) decreased stability of the alloy under the cell potentials in acidic electrolytes [189]. The use of multiple leaching processes prior to assembly was shown to be effective in Ref. [189].

Keeping into consideration the interaction between the catalyst and its support and the effect of structural modifications on the activity and the durability of the catalyst, surface functionalization is utilized. Nitrogen functionalization and its effects on the interaction of the catalyst-carbon support are especially researched [197−199].

6. Characterization of the catalyst layer

Characterization of the catalyst layer can be done either ex- or in-situ. Basic analysis of the CL structure involves porosimetric analysis to determine the pore size and its distributions, SEM analysis to evaluate agglomerate size and distribution and TEM analysis for Pt particle and ionomer distribution. In situ analyses involve the use of electrochemical characterization techniques to investigate the kinetics and mass transport resistances within the CL. Mainly, this involves the use of cyclic voltammetry (CV) to

determine the electrochemical surface area of the catalyst, linear sweep voltammetry (LSV) to determine gas crossover, electrochemical impedance spectroscopy (EIS) to determine protonic conductivity, polarization curve analyses under high oxygen stoichiometry to determine the ORR kinetics and under load to evaluate the mass transport resistance. In this part of the paper, we give an overview of various characterization techniques utilized in the study of catalyst layers.

6.1. Electrochemical techniques

6.1.1. Polarization curves

In order to investigate the performance of the catalyst layer with various Nafion loadings, Antolini et al. [26] fitted their polarization curves according to:

$$E = E_r + b \log i^\circ - b \log i - R_u i \tag{6}$$

where E_r is the reversible potential for the electrode, b is the Tafel slope, i° is the exchange current density for the ORR in the Pt/C catalyst and R_u represents the total contributions of the polarization components in the linear region of the polarization curve, which include the electron transfer resistance, the resistance of the electrolyte and the mass transfer resistance due to the gas crossing through the diffusion and catalytic layers.

6.1.2. Cyclic voltammetry

Cyclic voltammetry (CV) is utilized to estimate the electrochemical active surface area (ECSA) and the double layer capacitance (C_{DL}). As the name of the technique suggests, the potential of the fuel cell is swept back and forth between two set voltage limits and the current is recorded. The potential scanning rate is linear with time and in most studies is in the range of $1–1000$ mV s^{-1} [200]. A lower sweep rate (e.g. 10 mV s^{-1}) is, however, preferred in order to minimize impedance losses in the porous electrodes [3]. To record a CV, the cell is often fed with hydrated hydrogen at one electrode, which acts as both the counter and reference electrode. The other side of the cell, the working electrode, is flushed with an inert gas, often nitrogen. The cycle is repeated until no change in the CV shape is observed. In a normal CV, once the voltage sweeps past a potential that is related to an active electrochemical reaction, the resultant current will increase, creating a peak. The current will then stabilize once all available reactants have been completely consumed. On the reverse voltage scan, the reverse electrochemical reaction may be observed. A typical CV plot is given in Fig. 7(a) and (b).

The ECSA of the Pt catalyst can be calculated from the charge density, q_{pt} (C cm^{-2}electrode), obtained from the CV experiment, the charge required to reduce a monolayer of protons on Pt, $\Gamma = 210$ μC cm^{-2}Pt [202] and the Pt content or loading in the electrode, L in g$_{pt}$ cm^{-2}electrode:

$$ECSA\left(cm_{pt}^2\, g_{pt}^{-1}\right) = \frac{q_{pt}}{\Gamma.L} \tag{7}$$

In reality, not all the catalyst is accessible to the reactants. Hence, one is often interested in the utilization of the catalyst. The utilization is calculated as a ratio of the ECSA to the specific area of the catalyst obtained by the catalyst manufacturer using chemisorption.

The double layer capacitance, C_{dl}, can also be obtained for the CV in terms of the charging current, i_{dl}, and the scan rate, v (V s^{-1}), as follows:

$$i_{dl} = C\frac{dE}{dt} = C_{dl}.v \tag{8}$$

The current used in Equation (8) is the current at potentials between 0.4 and 0.6 V and it is the sum of the capacitive current due to charging/discharging of the electrical double layer and the transport limited H_2 crossover current.

Although cyclic voltammetry is a well-established technique to measure the electrochemical active surface area of an electrode, one must be aware of the artifacts that can arise due to the measurement methodology. In Ref. [203], Carter et al. discussed spatially resolved CV measurements and illustrated their dependency on nitrogen purge flow rate on the working electrode during the voltage sweep. Artifacts due to hydrogen evolution on the working electrode can arise and can be mitigated by reducing the purse rate to below 1 sccm cm^{-2} [203].

6.1.3. Linear sweep voltammetry

Linear sweep voltammetry (LSV) is used to determine the fuel crossover rate. Similarly to CV, LSV is run using an inert gas, e.g. nitrogen, on the cathode, while hydrogen is supplied to the fuel cell anode. The potential of the cathode is swept by means of a linear potential scan to potentials at which any hydrogen gas present at the cathode is instantaneously oxidized. The potential is scanned from 0.1 V to 0.8 V as shown in Fig. 7(c). The crossover flux, $J_{x-over,H2}$ (mol cm^{-2} s^{-1}) is obtained as follows:

$$J_{x-over,H2} = \frac{i_{lim}}{n.F} \tag{9}$$

where i_{lim} is the transport limiting current density (A cm^{-2}), n is the number of electrons taking part in the reaction and F is Faraday's constant 96,485 (C electron-mole^{-1}). As is seen from Fig. 7(c) the current can attain either a constant or linearly increasing value with increasing electrode potential. An increasing value of the current is indicative of a resistance due to internal shorting. This resistance is calculated based on the slope of the voltage versus current plot.

6.1.4. Electrochemical impedance spectroscopy

Electrochemical impedance spectroscopy (EIS) is measured based on the linear response theory, which implies that the system response to an interfering signal is linear. To ensure this linearity holds, it is important to select a small amplitude of interfering signal, $\hat{i}$. As a rule of thumb, $2–5\%$ of the DC signal value is often used as the perturbing signal in galvanostatic mode [205] and <10 mV in potentiostatic mode. The cell must reach a steady state before an EIS measurement can be carried out.

Impedance spectroscopy is often run in the frequency range of 10,000 Hz–0.1 Hz. Plotting the resultant imaginary impedance against its real counterpart results in a plot referred to as the Nyquist plot. Proton resistance of the catalyst layer can be estimated from the Nyquist plot of a H_2/N_2 cell. The Nyquist plot usually has two characteristic slopes: (1) at ~45° angle in the high frequency region due to proton resistance in the CL and (2) at an angle between 55°–90° at lower frequencies dominated by the capacitance of the CL. Extrapolating the second slope to the real impedance axis, Z' axis, the proton resistance, R_p, can be found from Ref. [206]:

$$R_p = 3\left(Z'_{LF} - Z'_{H,F}\right) \tag{10}$$

where $Z'_{H,F}$ is the high frequency intercept at the real part of the impedance and Z'_{LF} is the extrapolated value of the intercept at the low frequency.

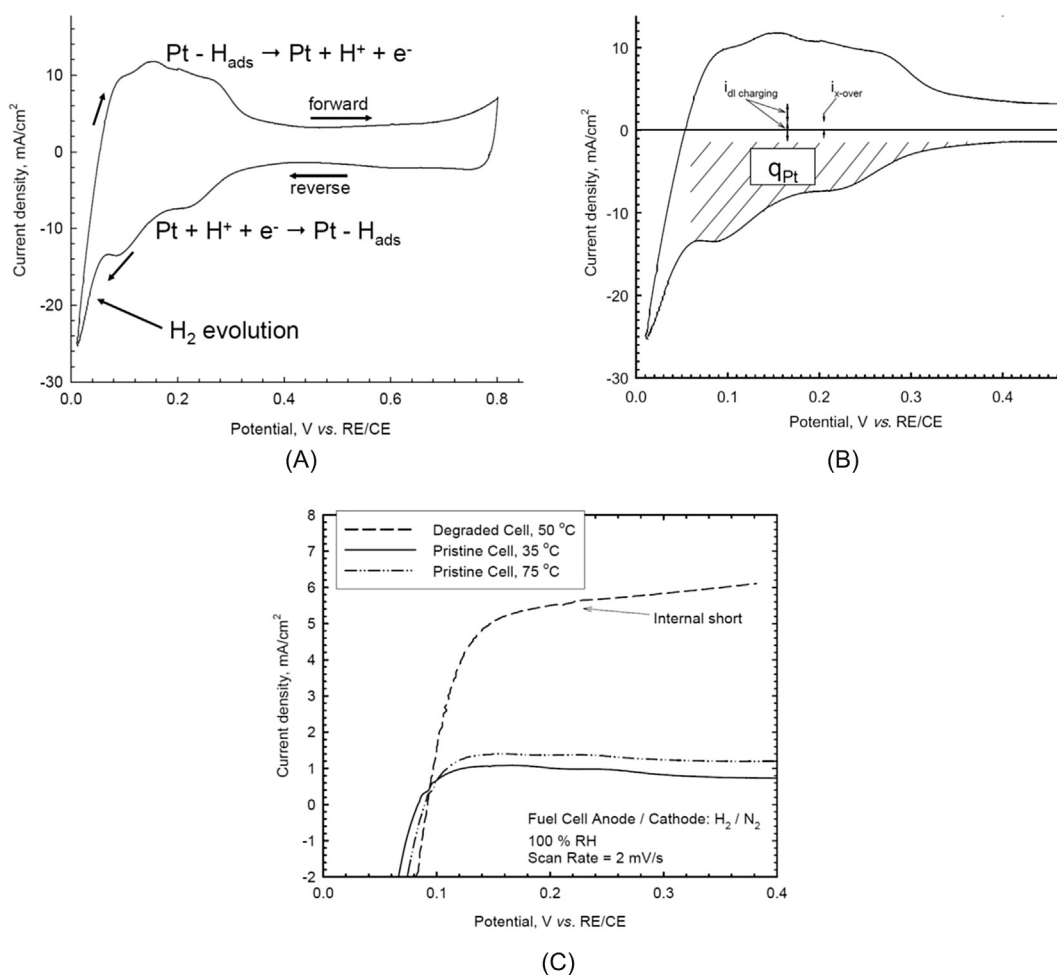The double layer capacitance is related to the proton resistance as follows [207]:

Fig. 7. (a) Cyclic voltammogram of PEM fuel cell catalyst layer for ECSA analysis by hydrogen adsorption/desorption *Reproduced from Ref. [201] with permission from Scribner Associates, Inc*; (b) Cyclic voltammogram of a PEMFC catalyst layer highlighting the region of interest. The shaded area is the charge density due to H adsorption during the reverse scan and is used in the ECSA calculation *Reproduced from Ref. [201] with permission from Scribner Associates, Inc*; (c) Linear sweep voltammograms for hydrogen crossover in a PEMFC−crossover flux of a pristine cell is around 1.1–1.4 mA/cm^2 *Reproduced from Ref. [204] with permission from Scribner Associates, Inc.*

$$Z = \sqrt{\frac{R_p}{C_{dl}}}\omega^{-0.5} \tag{11}$$

where $\omega = 2\pi f$ is the frequency. Usually, a frequency in the range of 1×10^4 to 1×10^3 Hz is used for the above analysis.

The membrane resistance can be obtained using EIS by running the cell with H_2/Air. The membrane resistance + contact and all electrical resistances are often referred to as the high frequency resistance as it is the intercept at the high frequency of the real impedance part of the Nyquist plot.

6.2. Physical techniques

6.2.1. Imaging techniques

It is of interest to investigate, visually, the interaction between the various components of the catalyst ink. There are various techniques used in the literature depending on the overall objective of the study. Some of the techniques used in the literature are summarized below.

i. The interaction between carbon black and Nafion ionomer in the catalyst ink has been investigated using cryogenic transmission electron microscopy in Ref. [208]. This method is employed often for the characterization of colloidal drug delivery systems; see Ref. [209].

ii. Identical location transmission electron microscopy has been used by Hartl et al. [210,211] to image the degradation process within the catalyst layer.

iii. Focused ion beam/scanning electron microscope (FIB/SEM) has been used to create 3-dimensional reconstruction of the catalyst layer; see Ref. [212]. With this technique 2-dimensional images at of the catalyst layer at various depths are collected and its morphology reconstructed.

iv. Combination of scanning electron microscope tomography (SEMt) and transmission electron microscopy tomography (TEMt) was applied to integrate information from both methods in Ref. [213]. With SEMt analysis, information in regards to the preferential size in the grain size distribution of about 65 nm and the pore size distribution can be gathered. While from TEMt, one can investigate the Pt particles size, distribution and shapes. With this knowledge, the authors suggested that information in regards to the reaction centers can be identified. A combination of SEM and TEM was also used in Ref. [214] to investigate the distribution of Pt particles on the carbon support. In Ref. [214], the authors investigated the effect of synthesis method on Pt deposition. Using the same carbon support, they found that the synthesis

process affects the deposition of Pt and consequently its utilization under various relative humidity conditions.

v. Soft x-ray radiography was used in Ref. [215] to visualize liquid water in the cathode catalyst layer.

vi. Scanning Transmission Soft X-ray Spectrotomography has been used in Refs. [216–218] to image the interaction between the carbon-support/catalyst and ionomer. This technique provides a means of probing the occupied density (OD) of electronic states of a material. In the case of the catalyst layer, the interest is in obtaining the OD of C 1s and F 1s as they provide information of the carbon distribution and the fluorine rich ionomer, respectively. An example of how this technique was used to reconstruct the ionomer/carbon distribution in the catalyst layer is given in Fig. 8.

6.2.2. Ionic resistance techniques

Techniques to measure the ionic resistance of the CL have been reviewed by Karan in Ref. [42]. In the literature, authors use three main methods to carry out such measurements, (i) AC impedance-based method, (ii) hydrogen-pump based DC resistance method and (iii) in-situ potential distribution method. The AC impedance was described earlier in Section 6.1.4 and relies on the use of a H_2/N_2 cell. The in-situ potential distribution method is that described in Ref. [45]. The hydrogen-pump method involves the use of a modified membrane electrode assembly configuration and the measurement of its resistance either by AC impedance or DC polarization measurements in a H_2/H_2 cell mode. This technique has been used by Boyer et al. and Iden et al. [43,219].

The application of inter-digitated electrodes (IDE) by impedance spectroscopy is used to measure the conductivity of ultra-thin ionomer films. Paul et al. [41] used this method to estimate the conductivity of thin Nafion films corresponding to 4, 30, 55 and 300 nm. In the same study, they investigated the effect of the relative humidity on the conductivity of these films. The authors found that the conductivity in mS cm^{-1} is exponentially dependent on the relative humidity as follows:

$$\sigma = 0.5159 exp(0.0661 \times RH\%) \quad \textit{for ionomer content } 5.0wt\%$$
(12 a)

$$\sigma = 0.5159 exp(0.1 \times RH\%) \quad \textit{for ionomer content } 0.1, \ 0.5, \ 1.0wt\%$$
(12 b)

6.2.3. Other characterization techniques

i. Dynamic Vapor Sorption (DVS) is a gravimetric technique for investigating water sorption/desorption on particulate materials. It is used to perform water vapor sorption experiments in catalyst layers; see Ref. [43]. Humidified nitrogen gas is often used in the characterization of the water uptake within membranes and catalyst layers in PEM fuel cells. With this measurement technique, the water content, λ, which represents the number of water molecules per sulfonic-acid group of ionomer can be determined as follows [54]:

$$\lambda = \frac{M_w / \overline{M_w}}{M_i^{dry} / EW}$$
(13)

where $M_w = M_{CL} - M_0$ is the weight of water adsorbed by the CL sample and is equal to the difference between the weight of the humidified CL sample and the initial weight of the CL. $\overline{M_w}$ is the molar weight of water (18 g mol^{-1}EW is the equivalent weight of the ionomer and $M_i^{dry} = \varepsilon_i M_{CL}$ is the dry weight of the ionomer in the CL sample and is the product of the ionomer content in the sample and the weight of the CL sample.

ii. Nitrogen physisorption is used to measure the specific surface area and the pore size distribution of the catalyst layer; see Ref. [24]. The method is based on Brunauer, Emmet and Teller theory (BET) and hence is often referred to in the fuel cell literature as BET N_2 adsorption. The specific surface area of a powder is estimated from the amount of nitrogen adsorbed in relationship with its pressure, at the boiling temperature of liquid nitrogen under normal atmospheric pressure.

iii. Hg intrusion can be used to characterize the pore size distribution and porosity of the CL; see Ref. [73].

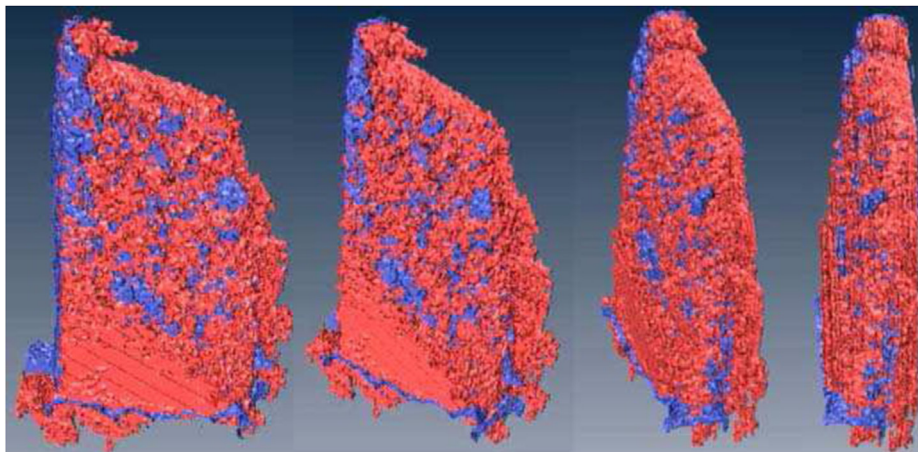iv. ICP, inductively coupled plasma, can be used to measure the Pt loading; see Ref. [24].

Fig. 8. Sample A: Simultaneous presentation of 3D chemical imaging of the carbon support (red) and ionomer (blue) components *Reproduced from Ref.* [217] *with permission from the Electrochemical Society.* (For interpretation of the references to colour in this figure legend, the reader is referred to the web version of this article.)

v. X-ray diffraction can be used to determine crystalline phases present in the catalyst layer. This technique has been used in Refs. [11,21] to determine the amount of Pt present in the NSTF catalyst layers.

vi. Ultra small angle x-ray scattering (USAXS) has been used in Ref. [208] to investigate the size and micro-geometry of aggregates in the catalyst ink.

vii. Grazing incidence small angle x-ray scattering (GISAXS) is used to investigate the surface morphology of ionomer films; see Ref. [56].

viii. Current sensing atomic force microscopy (AFM) is used for measuring the local conductivity of ionomer film samples; see Ref. [57].

ix. Environmental scanning electron microscope (ESEM) is used to evaluate the impact of phase change of water by cycling the water inside the catalyst layer between liquid-vapor-ice in Ref. [220]. The investigation was carried out for Pt/C dispersed catalyst layers as well as NSTF catalyst layers.

x. Electron spin resonance (ESR) spectroscopy is a means for estimating the number of unpaired electrons in a structure. At least two types of interactions are possible; physical and chemical. The physical interaction results in the broadening of the ESR signal and a decrease in its intensity and is attributed to magnetic interaction between the electrons without their actual pairing. If the unpaired electrons come together to form a bond chemically, then this chemical interaction results in a decrease in the signal of the ESR without its broadening. In the case of the catalyst layer, this type of technique is used to investigate the interaction between the catalyst and its support. ESR was used to investigate the electronic interaction between Pt and its carbon support in Ref. [180].

7. Conclusions

In this paper, an overview of the works tailored to understanding the transport mechanisms within the catalyst layer of PEM fuel cells was put forward. The focus of the discussion was to shed light on the current status of our understanding of how the various ingredients of the layer affect the durability and stability of the catalyst layer and ultimately the performance of the cell. It is clear that progress in the science of catalyst layer design is dependent on excellent electrode structuring where the catalyst is optimally dispersed in the layer and fully utilized, while the support is stable and the ionomer optimally creates the 3-phase interface without limiting oxygen transport. To achieve this goal, proper structuring of the catalyst layer is key. This is achievable through fundamental understanding of the catalyst layer morphology coupled with in- and ex-situ analysis of its performance. An example of this simple idea is the work by Gasteiger et al. where the Pt catalyst loading was reduced through the optimization of the layer's structure. In this case, through optimization, the Pt loading was successfully reduced from 0.40 to 0.20 mg_{Pt} cm^{-2} with cell voltage losses of only 20 mV [221].

Despite much work done on this topic, alternative supports to carbon and alternative catalysts to Pt are yet to prove to be commercially viable. The main obstacle for the use of these alternative materials is their reduced stability and ultimately reduced activity under the various operating conditions of PEM fuel cells. Hence, focus should be put towards how to utilize the high stability and activity of the Pt/C in the design of future catalyst layers. This should be approached from fundamental modelling to catalyst layer design and manufacturing. Throughout these efforts, engineering charts describing the performance dependency on various design parameters should be established to create a basis for the design of future catalyst layers where the performance can be predicted.

Acknowledgements

References

[1] Niedrach, US Patent 3,297,484 (1967).
[2] L.D. Raistrick, Diaphragms, separators, and ion exchange membranes, PV86-13, in: J.W. Van Zee, R.E. White, K. Kinoshita, H.S. Burney (Eds.), The Electrochemical Society Proceedings Series, Pennington, NJ, 1986, p. 172.
[3] E.A. Ticianelli, J.G. Berry, S. Srinivasan, J. Electroanal. Chem. 251 (1988) 275—295.
[4] M. Uchida, Y. Aoyama, N. Eda, A. Ohta, J. Electrochem. Soc. 142 (1995) 4143—4149.
[5] M.S. Wilson, S. Gottesfeld, J. Appl. Electrochem. 22 (1992) 1—7.
[6] M.S. Wilson, S. Gottesfeld, J. Electrochem. Soc. 139 (1992) L28—L30.
[7] K. More, R. Borup, K. Reeves, ECS Trans. 3 (2006) 717—733.
[8] S. Holdcroft, Chem. Mater. 26 (2014) 381—393.
[9] K. Malek, M. Eikerling, Q.P. Wang, T.C. Navessin, Z.S. Liu, J. Phys. Chem. C 111 (2007) 13627—13634.
[10] Z. Xia, Q. Wang, M. Eikerling, Z.S. Liu, Can. J. Chem. 86 (2008) 657—667.
[11] M.K. Debe, Novel catalysts, catalysts support and catalysts coated membrane methods, in: W. Vielstich, A. Lamm (Eds.), Handbook of Fuel Cells — Fundamentals Technology and Applications, John Wiley & Sons, Gasteiger HA, 2003 (Chapter 45).
[12] R. O'Hayre, S.J. Lee, S.W. Cha, F.B. Prinz, J. Power Sources 109 (2002) 483—493.
[13] D. Gruber, N. Ponath, J. Müller, F. Lindstaedt, J. Power Sources 150 (2005) 67—72.
[14] M.S. Saha, A.F. Gullá, R.J. Allen, S. Mukerjee, Electrochimica Acta 51 (2006) 4680—4692.
[15] X. Zhang, P. Shi, Electrochem. Commun. 8 (2006) 1229—1234.
[16] H.-N. Su, S.-J. Lao, Y.-N. Wu, J. Power Sources 195 (2010) 3477—3480.
[17] B. Zhao, L. Sun, R. Ran, Z. Shao, Solid State Ionics 262 (2014) 313—318.
[18] O.-H. Kim, Y.-H. Cho, S.H. Kang, H.-Y. Park, M. Kim, J.W. Lim, D.Y. Chung, M.J. Lee, H. Choe, Y.-E. Sung, Nat. Commun. 4 (2013) 2473—2482.
[19] Y. Liu, J. Chen, V. Misoska, G.F. Swiegers, G.G. Wallace, Mater. Lett. 61 (2007) 2887—2890.
[20] D. Yamamoto, H. Munakata, K. Kanamura, J. Electrochem. Soc. 155 (2008) B303—B308.
[21] M.K. Debe, A.K. Schmoeckel, G.D. Vernstrom, R. Atanasoski, J. Power Sources 161 (2006) 1002—1011.
[22] H. Zhang, X. Wang, J. Zhang, J. Zhang, Conventional catalyst ink, catalyst layer and MEA preparation, in: J. Zhang (Ed.), PEM Fuel Cell Electrocatalysts and Catalyst Layers — Fundamentals and Applications, Springer, 2008 (Chapter 19).
[23] J.H. Wee, K.Y. Lee, S.H. Kim, J. Power Sources 165 (2007) 667—677.
[24] T. Soboleva, X. Zhao, K. Malek, Z.S. Xie, T. Navessin, S. Holdcroft, ACS Appl. Mater. Interfaces 2 (2010) 375—384.
[25] G. Sasikumar, J.W. Ihm, H. Ryu, J. Power Sources 132 (2004) 11—17.
[26] E. Antolini, L. Giorgi, A. Pozio, P. Passalacqua, J. Power Sources 77 (1999) 136—142.
[27] G. Sasikumar, J.W. Ihm, H. Ryu, J. Power Sources 50 (2004) 601—605.
[28] E.A. Ticianelli, C.R. Berouin, A. Redondo, S. Srinivasan, J. Electrochem. Soc. 135 (1988) 2209—2214.
[29] Z. Poltarzewski, P. Staiti, V. Alderucci, W. Wieczorek, N. Giordano, J. Electrochem. Soc. 139 (1992) 761—765.
[30] V.A. Paganin, E.A. Ticianelli, E.R. Gonzalez, J. Appl. Electrochem. 26 (1996) 297—304.
[31] S.J. Lee, S. Mukerjee, J. McBreen, Y.W. Rho, Y.T. Kho, T.H. Lee, Electrochimica Acta 43 (1998) 3693—3701.
[32] J.M. Song, S.Y. Cha, W.M. Lee, J. Power Sources 94 (2001) 78—84.
[33] G. Li, P.G. Pickup, J. Electrochem. Soc. 150 (2003) C745—C752.
[34] J. Xie, F. Xu, D.L. Wood, K.L. More, T.A. Zawodzinski, W.H. Smith, Electrochimica Acta 55 (2010) 7404—7412.
[35] S. Sambandam, V. Ramani, Phys. Chem. Chem. Phys. 12 (2010) 6140—6149.
[36] S. von Kraemer, M. Puchner, P. Jannasch, A. Lundblad, G. Lindbergh, J. Electrochem. Soc. 153 (2006) A2077—A2084.
[37] S. Sambandam, J. Parrondo, V. Ramani, Phys. Chem. Chem. Phys. 15 (2013) 14994—15002.
[38] S. Kaliaguine, S.D. Mikhailenko, K.P. Wang, P. Xing, G. Robertson, M. Guiver, Catal. Today 82 (2003) 213—222.
[39] H.Y. Jung, K.Y. Cho, K.A. Sung, W.K. Kim, J.K. Park, J. Power Sources 163 (2006) 56—59.

[40] Z. Siroma, R. Kakitsubo, N. Fujiwara, T. Ioroi, S. Yamazaki, K. Yasuda, J. Power Sources 189 (2009) 994–998.
[41] D.K. Paul, A. Fraser, K. Karan, Electrochem. Commun. 13 (2011) 774–777.
[42] K. Karan, ECS Trans. 50 (2012) 395–403.
[43] T. Soboleva, K. Malek, Z. Xie, T. Navessin, S. Holdcroft, ACS Appl. Mater. Interfaces 3 (2011) 1827–1837.
[44] C. Boyer, S. Gamburzev, O. Velev, S. Srinivasan, A.J. Appleby, Electrochimica Acta 43 (1998) 3703–3709.
[45] K.C. Hess, W.K. Epting, S. Lister, Anal. Chem. 83 (2011) 9492–9498.
[46] T.A. Zawodzinski, C. Derouin, S. Radzinski, R.J. Sherman, V.T. Smith, T.E. Springer, S.J. Gottesfeld, J. Electrochem. Soc. 140 (1993) 1041–1047.
[47] K.T. Regner KT. (Master's thesis), Virginia Polytechnic Institute and State University 2011.
[48] Z. Ogumi, T. Kuroe, Z. Takehara, J. Electrochem. Soc. 132 (1985) 2601–2605.
[49] F.N. Büchi, M. Wakizoe, S. Srinivasan, J. Electrochem. Soc. 143 (1996) 927–932.
[50] T. Shimura, K. Miyatake, M. Watanabe, Eur. Polym. J. 44 (2008) 4054–4062.
[51] A. Ayad, J. Bouet, J.F. Fauvarque, J. Power Sources 149 (2005) 66–71.
[52] J.P. Owejan, J.E. Owejan, W. Gu, J. Electrochem. Soc. 160 (2013) F824–F833.
[53] B.S. Pivovar, Y.S. Kim, J. Electrochem. Soc. 154 (2007) B739–B744.
[54] A. Kongkanand, J. Phys. Chem. C 115 (2011) 11319–11325.
[55] A. Kusoglu, A. Kwong, K.T. Clarck, H.P. Gunterman, A.Z. Weber, J. Electrochem. Soc. 159 (2012) F530–F535.
[56] M.A. Modestino, A. Kusoglu, A. Hexemer, A.Z. Weber, R.A. Segalman, Macromolecules 45 (2012) 4681–4688.
[57] Q. He, A. Kusoglu, I.T. Lucas, K. Clark, A.Z. Weber, R. Kostecki, J. Phys. Chem. B 115 (2011) 11650–11657.
[58] V. Mehta, J.S. Cooper, J. Power Sources 114 (2003) 32–53.
[59] K. Prater, J. Power Sources 29 (1990) 239–250.
[60] G.A. Eisman, J. Power Sources 29 (1990) 389–398.
[61] S.M. Javaid Zaidi, Research trends in polymer electrolyte membranes for PEMFC, in: J. Zaidi, T. Matsuura (Eds.), Polymer Membranes for Fuel Cells, Springer, 2009.
[62] A. Ghielmi, P. Vaccarono, C. Troglia, V. Arcella, J. Power Sources 145 (2005) 108–115.
[63] M. Gebert, Aquivion™ – The short-side-chain and low-EW PFSA for next generation PEFCs expands production and utilization, in: Proceedings in: 18th World Hydrogen Energy Conference 2010, May 16-21, 2010 (Essen, Germany).
[64] K.D. Kreuer, M. Schuster, B. Obliers, O. Diat, U. Traub, A. Fuchs, U. Klock, S.J. Paddison, J. Maier, J. Power Sources 178 (2008) 499–509.
[65] S.J. Paddison, J.A. Elliott, Solid State Ionics 177 (2006) 2385–2390.
[66] S.J. Paddison, J.A. Elliott, Solid State Ionics 178 (2007) 561–567.
[67] J. Peron, D. Edwards, M. Haldane, X. Luo, Y. Zhang, S. Holdcroft, Z. Shi, J. Power Sources 196 (2011) 176–181.
[68] C. Lei, D. Bessarabov, S. Ye, Z. Xie, S. Holdcroft, T. Navessin, J. Power Sources 196 (2011) 6168–6176.
[69] H. Xu, H.R. Kunz, L.J. Bonville, J.M. Fenton, J. Electrochem. Soc. 154 (2007) B271–B278.
[70] N. Zhoa, D. Edwards, C. Lei, K. Wang, J. Li, Y. Zhang, S. Holdcroft, Z. Shi, J. Power Sources 242 (2013) 877–883.
[71] M.P. Rodgers, B.P. Pearman, N. Mohajeri, L.J. Bonville, D.K. Slattery, Electrochimica Acta 100 (2013) 180–187.
[72] S.J. Paddison, J.A. Elliott, Solid State Ionics 177 (2006) 2385–2390.
[73] S.J. Paddison, J.A. Elliott, Phys. Chem. Chem. Phys. 8 (2006) 2193–2203.
[74] X. Wu, K. Scott, V. Pthiyapura, Int. J. Hydrogen Energy 37 (2012) 13243–13248.
[75] J. Kerres, W. Zhang, L. Jörissen, V. Gogel, J. New Mater. Electrochem. Syst. 5 (2002) 97–107.
[76] Y.S. Kim, M.J. Sumner, W.L. Harrison, J.S. Riffle, J.E. McGrath, B.S. Pivovar, J. Electrochem. Soc. 151 (2004) A2150–A2156.
[77] H.Y. Jung, K.Y. Cho, K.A. Sung, W.K. Kim, J.K. Park, J. Power Sources 163 (2006) 56–59.
[78] E. Passalacqua, F. Lufrano, G. Squadrito, A. Patti, L. Giorgi, Electrochmica Acta 46 (2001) 799–805.
[79] Z. Qi, A. Kaufman, J. Power Sources 117 (2003) 37–43.
[80] K.H. Kim, K.Y. Lee, S.Y. Lee, E. Cho, T.H. Lim, H.J. Kim, S.P. Yoon, S.H. Kim, T.W. Lim, J.H. Jang, Int. J. Hydrogen Energy 35 (2010) 13104–13110.
[81] S. Jeon, J. Lee, G.M. Rios, H.J. Kim, S.Y. Lee, E. Cho, T.H. Lim, J.H. Jang, Int. J. Hydrogen Energy 35 (2010) 9678–9686.
[82] Y.S. Kim, C.F. Welch, N.H. Mack, R.P. Hjelm, E.B. Orler, M.E. Hawley, K.S. Lee, S.-D. Yim, C.M. Johnston, Phys. Chem. Chem. Phys. 16 (2014) 5927–5932.
[83] Y.S. Kim, C.F. Welch, R.P. Hjelm, N.H. Mack, A. Labouriau, E.B. Orler, Macromolecules 48 (2015) 2161–2172.
[84] D.C. Huang, P.J. Yu, F.J. Liu, S.L. Huang, K.L. Hsueh, Y.C. Chen, C.H. Wu, W.C. Chang, Fh Tsau, Int. J. Electrochem. Sci. 6 (2011) 2551–2565.
[85] Z. Xie, X. Zhao, M. Adachi, Z. Shi, T. Mashio, A. Ohma, K. Shinohara, S. Holdcroft, T. Navessin, Energy Environ. Sci. 1 (2008) 184–193.
[86] M. Chisaka, H. Diaguji, Electrochimica Acta 51 (2006) 4828–4833.
[87] K. Kinoshita, Carbon: Electrochemical and Physiochemical Properties, Wiley, New York, 1988.
[88] M. Eikerling, J. Electrochem. Soc. 153 (2006) E58–E70.
[89] Y. Liu, C. Ji, G. Wenbin, J. Jorne, H.A. Gasteiger, J. Electrochem. Soc. 158 (2011) B614–B621.
[90] M. Kim, J.N. Park, H. Kim, S. Song, W.H. Lee, J. Power Sources 163 (2006) 93–97.
[91] R. Borup, J. Meyers, B. Pivovar, Y.S. Kim, R. Mukundan, N. Garland, D. Myers, M. Wilson, F. Garzon, D. Wood, P. Zelenay, K. More, K. Stroh, T. Zawodzinski, J. Boncella, J. McGrath, M. Inaba, K. Miyatake, M. Hori, K. Ota, Z. Oqumi, S. Miyata, A. Nishikata, Z. Siroma, Y. Uchimoto, K. Yasuda, K. Kimijima, N. Iwashita, Chem. Rev. 107 (2007) 3904–3951.
[92] P.J. Ferreira, G.J. La O', Y. Shao-Horn, D. Morgan, R. Mkharia, S. Kocha, H.A. Gasteiger, J. Electrochem. Soc. 152 (2005) A2256–A2271.
[93] J. Wang, G. Yin, Y. Shao, S. Zhang, Z. Wang, Y. Gao, J. Power Sources 171 (2007) 331–339.
[94] K.E. Swider, D.R. Rolison, J. Electrochem. Soc. 143 (1996) 813–819.
[95] S.C. Roy, A.W. Harding, A.E. Russell, K.M. Thomas, J. Electrochem. Soc. 144 (1997) 2323–2328.
[96] G. Siné, G. Fóti, Ch. Comninellis, J. Electroanal. Chem. 595 (2006) 115–124.
[97] G.R. Salazar-Banda, H.B. Suffredini, M.L. Calegaro, S.T. Tanimoto, L.A. Avaca, J. Power Sources 162 (2006) 9–20.
[98] H.B. Suffredini, V. Tricoli, N. Vatistas, L.A. Avaca, J. Power Sources 158 (2006) 124–128.
[99] N.R. Stradiotto, K.E. Toghill, L. Siao, A. Moshar, R.G. Compton, Electroanalysis 21 (2009) 2627–2633.
[100] N. Spâtaru, X. Zhang, T. Spâtaru, D.A. Tryk, A. Fujishima, J. Electrochem. Soc. 155 (2008) B264–B269.
[101] M.C. Granger, M. Witek, J. Xu, J. Wang, M. Hupert, A. Hanks, M.D. Koppang, J.E. Butler, G. Lucazeau, M. Mermoux, J.W. Strojek, G.M. Swain, Anal. Chem. 72 (2000) 3793–3804.
[102] R.G. Compton, J.S. Foord, F. Marken, Electroanalysis 15 (2003) 1349–1363.
[103] T. Yano, D.A. Tryk, K. Hashimoto, A. Fujishima, J. Electrochem. Soc. 145 (1998) 1870–1876.
[104] G.R. Salazar-Banda, K.I.B. Equiluz, L.A. Avaca, Electrochem. Commun. 9 (2007) 59–64.
[105] F. Montilla, E. Morallón, I. Duo, Ch Comninellis, J.L. Vázquez, Electrochimica Acta 48 (2003) 3891–3897.
[106] X. Lyu, J. Hu, J.S. Foord, Q. Wang, J. Power Sources 242 (2013) 631–637.
[107] M. Paunovic, M. Schlesinger, Fundamentals of Electrochemical Deposition, Wiley, New York, 1998.
[108] J. Kim, Y.S. Chun, S.K. Lee, D.S. Lim, RSC Adv. 5 (2015) 1103–1108.
[109] K.P. De Jong, J.W. Geus, Catal. Rev. – Sci. Eng. 42 (2000) 481–510.
[110] D. Sebastián, I. Suelves, M.J. Lázaro, R. Moliner, J. Power Sources 192 (2009) 51–56.
[111] L. Calvillo, M.J. Lázaro, I. Suelves, Y. Echegoyen, E.G. Bordejé, R. Moliner, J. Nanosci. Nanotechnol. 9 (2009) 4161–4169.
[112] D. Sebastián, I. Suelves, R. Moliner, M.J. Lázaro, Carbon 48 (2010) 4421–4431.
[113] Z.R. Ismagilov, M.A. Kerzhenstev, N.V. Shikina, A.S. Lisitsyn, L.B. Okhlopkova, ChN. Bamkov, M. Sakashita, T. Iijima, K. Tadokoro, Catal. Today 102–103 (2005) 58–66.
[114] F. Yuan, H.K. Yu, H. Ryu, Electrochimica Acta 50 (2004) 685–691.
[115] A. Guha, W. Lu, T.A. Zawodzinski Jr., D.A. Schiraldi, J. Power Sources 172 (2007) 530–541.
[116] L. Calvillo, M. Gangeri, S. Perathoner, G. Centi, R. Moliner, M.J. Lázaro, J. Power Sources 192 (2009) 144–150.
[117] G. Álvarez, F. Alcaide, P.L. Cabot, M.J. Lázaro, E. Pastor, J. Solla-Gullón, Int. J. Hydrogen Energy 37 (2012) 393–404.
[118] J. Wang, Y. Chen, Y. Zhang, I. Ionescu, R. Li, X. Sun, S. Ye, S. Knights, J. Mater. Chem. 21 (2011) 18195–18198.
[119] J.S. Zheng, X.S. Zhang, P. Li, J. Zhu, X.G. Zhou, W.K. Yuan, Electrochem. Commun. 9 (2007) 895–900.
[120] G. Che, B.B. Lakshmi, E.R. Fisher, C.R. Martin, Nature 393 (1998) 346–349.
[121] Z. Liu, X. Lin, J.Y. Lee, W. Zhang, M. Han, L.M. Gan, Langmuir 18 (2002) 4054–4060.
[122] E. Antolini, Appl. Catal. B Environ. 74 (2007) 337–350.
[123] C.H. Wang, H.Y. Du, Y.T. Tsai, C.P. Chen, C.J. Huang, L.C. Chen, K.H. Chen, H.C. Shih, J. Power Sources 171 (2007) 55–62.
[124] V. Bagilo, A. Di Blasi, C. D'Urso, V. Antonucci, A.S. Aricò, R. Ornelas, D. Morales-Acosta, J. Ledesma-Garcia, L.A. Godinez, L.C. Arriaga, L. Alvarez-Contreras, J. Electrochem. Soc. 155 (2008) B829–B833.
[125] L. Gan, R. Lv, H. Du, B. Li, F. Kang, Electrochem. Commun. 11 (2009) 355–358.
[126] E.S. Steigerwalt, G.A. Deluga, D.E. Cliffel, C.M. Lukehart, J. Phys. Chem. B 105 (2001) 8097–8101.
[127] C.A. Bessel, K. Laubernds, N.M. Rodriguez, R.T.K. Baker, J. Phys. Chem. B 105 (2001) 1115–1118.
[128] S.N. Stamatin, M. Borghei, S.M. Andersen, S. Veltze, V. Ruiz, E. Kauppinen, E.M. Skou, Int. J. Hydrogen Energy 39 (2014) 8215–8224.
[129] X. Wang, S. Wang, Catalyst support materials for proton exchange membrane fuel cells (Chapter 3), in: B. Ladewig, S.P. Jiang, Y. Yan, M. Lu (Eds.), Materials for Low Temperature Fuel Cells, Wiley, 2015.
[130] O. Ikeda, K. Okabayashi, N. Yoshida, H. Tamura, J. Electroanal. Chem. 191 (1985) 157–174.
[131] M. Fabrizio, G. Mengoli, M.M. Musiani, F. Paolucci, J. Electroanal. Chem. 300 (1991) 23–34.
[132] C.S.C. Bose, K. Rajeshwar, J. Electroanal. Chem. 333 (1992) 235–256.
[133] C.C. Chen, C.S.C. Bose, K. Rajeshwar, J. Electroanal. Chem. 350 (1993) 161–176.
[134] C. Coutanceau, A.E. Hourch, P. Crouigneau, J.M. Leger, C. Lamy, Electrochimica Acta 40 (1995) 2739–2748.
[135] H. Laborde, J.M. Leger, C. Lamy, F. Garnier, A. Yassar, J. Appl. Electrochem. 20

[136] Z. Qi, M.C. Lefebvre, P.G. Pickup, J. Electroanal. Chem. 459 (1998) 9–14.
[137] B. Rajesh, K.R. Thampi, J.M. Bonard, H.J. Mathieu, N. Xanthopoulos, B. Viswanathan, Electrochem. Solid-State Lett. 7 (2004) A404–A407.
[138] H.H. Zhou, S.Q. Jiao, J.H. Chen, W.Z. Wei, Y.F. Kuang, J. Appl. Electrochem. 34 (2004) 455–459.
[139] B. Rajesh, K.R. Thampi, J.M. Bonard, A.J. McEvory, N. Xanthopoulos, H.J. Mathieu, B. Viswanathan, J. Power Sources 133 (2004) 155–161.
[140] T. Maiyalagan, J. Power Sources 179 (2008) 443–450.
[141] W. Gao, L.B. Alemany, L. Ci, P.M. Ajayan, Nat. Chem. 1 (2009) 403–408.
[142] S. Guo, S. Dong, E. Wang, ACS Nano 4 (2010) 547–555.
[143] S. Liu, J. Wang, J. Zeng, J. Ou, Z. Li, X. Liu, S. Yang, J. Power Sources 195 (2010) 4628–4633.
[144] L. Qu, Y. Liu, J.B. Baek, L. Dai, ACS Nano 4 (2010) 1321–1326.
[145] Y. Li, W. Gao, L. Ci, C. Wang, P.M. Ajayan, Carbon 48 (2010) 1124–1130.
[146] N. Soin, S.S. Roy, T.H. Lim, J.A.D. McLaughlin, Mater. Chem. Phys. 129 (2011) 1051–1057.
[147] H. Gao, L. Song, W. Guo, L. Huang, D. Yang, F. Wang, Y. Zuo, X. Fan, Z. Liu, W. Gao, R. Vajtai, K. Hackenberg, P.M. Ajayan, Carbon 50 (2012) 4476–4482.
[148] H. Chhina, S. Campbell, O. Kesler, J. Electrochem. Soc. 156 (2009) B1232–B1237.
[149] T. Matsui, T. Okanishi, K. Fujiwara, K. Tsutsui, R. Kikuchi, T. Takeguchi, K. Eguchi, Sci. Technol. Adv. Mater. 7 (2006) 524–530.
[150] I.S. Park, E. Lee, A. Manthiram, J. Electrochem. Soc. 157 (2010) B251–B255.
[151] L. Wang, D.M. Xing, Y.H. Liu, Y.H. Cai, Z.G. Shao, Y.F. Zhai, H.X. Zhong, B.L. Yi, H.M. Zhang, J. Power Sources 161 (2006) 61–67.
[152] M. Nie, P.K. Shen, Z. Wei, J. Power Sources 167 (2007) 69–73.
[153] Y. Suzuki, A. Ishihara, S. Misushima, N. Kamiya, K.I. Ota, Electrochem. Solid-State Lett. 10 (2007) B105–B107.
[154] S. Sharma, B.G. Pollet, J. Power Sources 208 (2012) 96–119.
[155] M.K. Debe, S.M. Hendricks, A.K. Schmoekel, R.T. Atanasoski, G.D. Vernstrom, G.M. Haugen. Durability aspects of nanostructured thin film catalysts for PEM fuel cells. ECS Transactions, vol. 1, Durability and Reliability of Low Temperature Fuel Cells Systems, 208th ECS Meeting.
[156] M.K. Debe, A.J. Steinbach, K.A. Lewinski, G.M. Haugen, G.D. Vernstrom, R.T. Atanasoski, A.E. Hester, P.L. Turner, R.J. Ziegler, J.M. Larson, M.T. Hicks, P.E. Serim, Activities of Low Pt Loading Carbon Less, Ultra-thin Nano-structured Film Based Electrodes for PEM Fuel Cells, and Performances in Roll Good Fabricated MEAs in Single Cells and Stacks, Fuel Cell Seminar, Miami, FL, November 3–6, 2003.
[157] M.K. Debe, Advanced catalyst membrane technology with enhanced performance and durability for automotive requirements, in: Proceedings of the 4th International Fuel Cell Workshop, Kofu, Japan, September 22–24, 2005.
[158] M.K. Debe, VII.A.2 Advanced MEAs for enhanced operating conditions, in: DOE Hydrogen, Fuel Cells and Infrastructure Technologies Program FY, 2005 (Progress report).
[159] M.K. Debe, J. Electrochem. Soc. 160 (2013) F522–F534.
[160] A. Kongkanand, J.E. Owejan, S. Moose, M. Dioguardi, M. Biradar, R. Makharia, J. Electrochem. Soc. 159 (2012) F676–F682.
[161] K. Chan, M. Eikerling, J. Electrochem. Soc. 158 (2011) B18–B28.
[162] P.K. Sinha, W. Gu, A. Kongkanand, E. Thompson, J. Electrochem. Soc. 158 (2011) B831–B840.
[163] F. Hasché, M. Oezaslan, P. Strasser, Phys. Chem. Chem. Phys. 12 (2010) 15251–15258.
[164] A. Kongkanand, P.K. Sinha, J. Electrochem. Soc. 158 (2011) B703–B711.
[165] A.J. Steinbach, M.K. Debe, M.J. Pejsa, D.M. Peppin, A.T. Haug, M.J. Kurkowski, S.M. Hendricks, ECS Trans. 41 (2011) 449–457.
[166] K.Y. Chen, P.K. Shen, A.C.C. Tseung, J. Electrochem. Soc. 142 (1995) L85–L86.
[167] M. Götz, H. Wendt, Electrochimica Acta 43 (1998) 3637–3644.
[168] B.N. Grgur, N.M. Markovic, P.N. Ross Jr., J. Electrochem. Soc. 146 (1999) 1613–1619.
[169] S. Mukerjee, S.J. Lee, E.A. Ticianelli, J. McBeen, B.N. Grgur, N.M. Markovic, et al., Electrochem. Solid State Lett. 2 (1999) 12–15.
[170] A. Lima, C. Coutanceau, J.M. Léger, C. Lamy, J. Appl. Electrochem. 31 (2001) 379–386.
[171] P. Liu, A. Logadottir, J.K. Nørskov, Electrochimica Acta 48 (2003) 3731–3742.
[172] C. Dupont, Y. Jugnet, D. Loffreda, J. Am. Chem. Soc. 128 (2006) 9129–9136.
[173] A.C. Garcia, V.A. Paganin, E.A. Ticianelli, Electrochimica Acta 53 (2008) 4309–4315.
[174] D.C. Papageorgopoulos, M. Keijzer, J.B.J. Veldhuis, F.A. de Bruijn, J. Electrochem. Soc. 149 (2002) A1400–A1404.
[175] Y.-H. Cho, B. Choi, Y.-H. Cho, H.-S. Park, Y.-E. Sung, Electrochem. Commun. 9 (2007) 378–381.
[176] N. Zamel, X. Li, Prog. Energy Combust. Sci. 37 (2011) 292–329.
[177] S. Srinivasan, Chapter 5: electrocatalysis of fuel cell reactions, in: Fuel Cells

[178] E. Principi, A. Witkowska, S. Dsoke, R. Marassi, A. Di Cicco, Phys. Chem. Chem. Phys. 11 (2009) 9987–9995.
[179] G.E. Ramirez-Caballero, P.B. Balbuena, J. Phys. Chem. C 113 (2009) 7851–7856.
[180] L.J. Hillenbrand, J.W. Lacksonen, J. Electrochem. Soc. 112 (1965) 249–252.
[181] J. Escard, C. Leclère, J.P. Contour, J. Catal. 29 (1973) 31–39.
[182] H. Zeliger, J. Electrochem. Soc. 114 (1967) 144–145.
[183] J. Bett, J. Lundquist, E. Washington, P. Stonehart, Electrochimica Acta 18 (1973) 343–348.
[184] K.F. Blurton, P. Greenburg, G.H. Oswin, D.R. Rutt, J. Electrochem. Soc. 119 (1972) 559–564.
[185] L.J. Bregoli, Electrochimica Acta 23 (1978) 489–492.
[186] M. Peuckert, T. Yoneda, R.A. Dalla Betta, M. Boudart, J. Electrochem. Soc. 133 (1986) 944–947.
[187] S. Mukerjee, J. Appl. Electrochem. 20 (1990) 537–548.
[188] M.K. Debe, Nature 486 (2012) 43–51.
[189] H.A. Gasteiger, S.S. Kocha, B. Sompalli, F.T. Wagner, Appl. Catal. B Environ. 56 (2005) 9–35.
[190] Fuel Cell Technical Team Roadmap – USDrive (2013). energy.gov/sites/prod/files/2014/02/f8/fctt_roadmap_june2013.pdf.
[191] M. Oezaslan, P. Strasser, J. Power Sources 196 (2011) 5240–5249.
[192] S. Koh, N. Hahn, C. Yu, P. Strasser, J. Electrochem. Soc. 155 (2008) B1281–B1288.
[193] P. Mani, R. Srivastava, P. Strasser, J. Power Sources 196 (2011) 666–673.
[194] K.C. Neyerlin, H.A. Gasteiger, C.K. Mittelsteadt, J. Jorne, W. Gu, J. Electrochem. Soc. 152 (2005) A1073–A1080.
[195] K.C. Neyerlin, W. Gu, J. Jorne, A. Clark Jr., H.A. Gasteiger, J. Electrochem. Soc. 154 (2007) B279–B287.
[196] E.L. Thompson, J. Jorne, H.A. Gasteiger, J. Electrochem. Soc. 154 (2007) B783–B792.
[197] G. Bae, D.H. Youn, S. Han, J.S. Lee, Carbon 51 (2013) 274–281.
[198] S. Pylypenko, A. Queen, T.S. Olson, A. Dameron, K. O'Neil, K.C. Neyerlin, B. Pivovar, H.N. Dinh, D.S. Ginley, T. Gennett, R. O'Hayre, J. Phys. Chem. C 115 (2011) 13667–13675.
[199] S. Pylypenko, A. Queen, T.S. Olson, A. Dameron, K. O'Neil, K.C. Neyerlin, B. Pivovar, H.N. Dinh, D.S. Ginley, T. Gennett, R. O'Hayre, J. Phys. Chem. C 115 (2011) 13676–13684.
[200] Z. Qi, Electrochemical methods for catalyst activity evaluation, in: J. Zhang (Ed.), PEM Fuel Cell Electrocatalysts and Catalyst Layers: Fundamentals and Applications, Springer, 2008.
[201] K.R. Cooper, In situ PEM fuel cell electrochemical surface area and catalyst utilization measurement, Fuel Cell Mag. (2009 Jan./Feb) 1–3.
[202] F. Gloaguen, J.M. Leger, C. Lamy, J. Appl. Electrochem. 27 (1997) 1052–1060.
[203] R.N. Carter, S.S. Kocha, F.T. Wagner, M. Fay, H.A. Gasteiger, ECS Trans. 11 (2007) 403–410.
[204] K.R. Cooper, In situ PEMFC fuel crossover and electrical short circuit measurement, Fuel Cell Mag. (2008 Aug./Sep) 1–2.
[205] X.Z. Yuan, C. Song, H. Wang, J. Zhang, Electrochemical Impedance Spectroscopy in PEM Fuel Cells: Fundamentals and Applications, Springer, 2010.
[206] K.R. Cooper, V. Ramani, J.M. Fenton, R. Kunz, Experimental Methods and Data Analysis for Polymer Electrolyte Fuel Cells, Scribner Associates, 2005.
[207] A. Hayránek, K. Wippermann, J. Electroanal. Chem. 567 (2004) 305–315.
[208] F. Xu, H.Y. Zhang, D. Ho, J. Ilavsky, M. Justics, H. Petrache, L. Stanciu, J. Xie, ECS Trans. 41 (2011) 637–645.
[209] J. Kuntsche, J.C. Horst, H. Bunies, Int. J. Pharm. 417 (2011) 120–137.
[210] K. Hartl, M. Hanzlik, M. Arenz, ECS Trans. 41 (2011) 811–816.
[211] K. Hartl, M. Hanzlik, M. Arenz, Energy Environ. Sci. 4 (2011) 234–238.
[212] C. Ziegler, S. Thiele, R. Zengerle, J. Power Sources 196 (2011) 2094–2097.
[213] S. Thiele, T. Fuerstenhaupt, D. Banham, T. Hutzenlaub, V. Birss, C. Ziegler, R. Zengerle, J. Power Sources 228 (2013) 185–192.
[214] K. Shinozaki, H. Yamada, Y. Morimoto, J. Electrochem. Soc. 158 (2011) B467–B475.
[215] P. Deevanhxay, T. Sasabe, S. Tsushima, S. Hirai, ECS Trans. 41 (2011) 403–408.
[216] V. Berejnov, D. Susac, J. Stumper, A.P. Hitchcock, ECS Trans. 41 (2011) 395–402.
[217] D. Susac, V. Berejnov, A.P. Hitchcock, J. Stumper, ECS Trans. 41 (2011) 629–635.
[218] V. Berejnov, D. Susac, J. Stumper, A.P. Hitchcock, ECS Trans. 50 (2012) 361–368.
[219] H. Iden, A. Ohma, K. Shinohara, ECS Trans. 16 (2008) 1751–1762.
[220] G.S. Hwang, H. Kim, R. Lujan, R. Mukundan, D. Spernjak, R.L. Borup, M. Kaviany, M.H. Kim, A.Z. Weber, Electrochimica Acta 95 (2013) 29–37.
[221] H.A. Gasteiger, J.E. Panels, S.G. Yan, J. Power Sources 127 (2004) 162–171.